

Three-field mixed finite element methods for nonlinear elasticity

Michael Neunteufel ^{*}, Astrid S. Pechstein [†] and Joachim Schöberl [‡]

Abstract

In this paper, we extend the tangential-displacement normal-normal-stress continuous (TDNNS) method from [25] to nonlinear elasticity. By means of the Hu–Washizu principle, the distributional derivatives of the displacement vector are lifted to a regular strain tensor. We introduce three different methods, where either the deformation gradient, the Cauchy–Green strain tensor, or both of them are used as independent variables. Within the linear sub-problems, all stress and strain variables can be locally eliminated leading to an equation system in displacement variables, only. The good performance and accuracy of the presented methods are demonstrated by means of several numerical examples (available via www.gitlab.com/mneunteufel/nonlinear_elasticity).

Keywords: mixed finite element method, nonlinear elasticity, large deformation

Introduction

The construction of discretization methods in elasticity is an active field of research. Mixed finite element methods entail a large variety of beneficial attributes compared to standard finite elements, which suffer from volume locking in the nearly incompressible regime and shear locking for flat elements. As an example of a mixed method, the Hellinger–Reissner formulation introduces the stress as a second, independent variable. For linear problems, there is a well established mathematical framework for analyzing stability and robustness properties, see the monograph by Boffi, Brezzi and Fortin [10]. The application of Hellinger–Reissner mixed methods to nonlinear problems is limited. Another classical mixed approach, the so-called Hu–Washizu or three-field approach, dates back to [47]. Here, the strain is used as a third field, which allows to treat a large class of nonlinear problems.

A basic principle of mixed formulations is integration by parts, which moves derivatives from the displacement to the stress field. Thus, higher continuity of the approximation space for the stress is required. The construction of symmetric matrix-valued finite elements with continuous normal components is non-trivial. Simplicial elements for the mixed Hellinger–Reissner formulation in two and three space dimensions have been constructed by Arnold and Winther [6] or Arnold, Awanou and Winther [3], respectively. As, especially in three dimensions, these elements are rather costly, different efficient variants have been introduced as elements with weak symmetry (e.g. [5, 46, 4]). In [25, 26, 27], the authors introduced and analyzed a Hellinger–Reissner formulation employing normal-normal continuous stress elements. This *tangential-displacement normal-normal-stress* (TDNNS) method for linear elasticity has been shown to be free from shear locking when discretizing thin structures by flat elements, and also robust when approaching the incompressible limit.

^{*}Corresponding author: Michael Neunteufel, Institute for Analysis and Scientific Computing, Technische Universität Wien, Wiedner Hauptstr. 8-10, 1040 Wien, Austria, email: michael.neunteufel@tuwien.ac.at

[†]Astrid S. Pechstein, Institute of Technical Mechanics, Johannes Kepler University Linz, Altenbergerstr. 69, 4040 Linz, Austria, email: astrid.pechstein@jku.at

[‡]Joachim Schöberl, Institute for Analysis and Scientific Computing, Technische Universität Wien, Wiedner Hauptstr. 8-10, 1040 Wien, Austria, email: joachim.schoeberl@tuwien.ac.at

In Hu–Washizu formulations, three independent fields are introduced – in the linear case, these three fields are comprised of displacement, strain, and stress, see also [13]. Different three-field formulations using an additional *enhanced strain* have been proposed in the literature: we cite the works by Simo and Rifai [44] and Kasper and Taylor [19]. Therein, the strain is assumed to decompose additively into a compatible part, associated with the displacement field, and an enhanced part. These methods were proven to be stable and efficient by various patch tests and benchmark problems. Reddy and Simo [31] also provided rigorous stability and convergence proofs for their elements.

The enhanced strain method from [44] has been extended to nonlinear elasticity by Simo, Armero and Taylor [43, 41]. Earlier, a mixed formulation based on the Hu–Washizu principle including finite-deformation elasto-plasticity was proposed by Simo, Taylor and Pister [42]. Kasper and Taylor [20] proposed a non-linear mixed-enhanced method with independent deformation gradient and first Piola–Kirchhoff stress. More recently, different groups introduced methods based on polyconvex strain energy-functions, where the deformation gradient, cofactor matrix and determinant are treated separately: we cite Pfeifferkorn and Betsch [29], Schröder, Wriggers and Balzani [39], and Bonet, Gil and Ortigosa [11, 12].

Reese, Wriggers and Reddy [35] introduced a reduced-integration stabilized brick element for finite elasticity, where the stabilization is based on the enhanced strain method. Later, Reese [33] proposed a brick solid-shell element based on reduced integration and hourglass stabilizations. More recently, a group around Reese proposed lowest-order locking-free hybrid discontinuous Galerkin elements for large deformations [49, 8]. The equivalence of this approach to hourglass stabilization and reduced integration was discussed in [34].

Angoshtari, Shojaei and Yavari [1] introduced the compatible-strain mixed finite element method (CSMFEMs) for two-dimensional compressible large deformation problems, which also belongs to the class of three-field formulations. Shojaei and Yavari later generalized this method to three dimensions and incompressible elasticity in [40, 40]. These elements are based on a Hilbert complex of nonlinear elasticity [2]: the displacement is chosen to be discretized with (conforming) nodal elements, its gradient by Nédélec and the first Piola–Kirchhoff stress tensor by Raviart–Thomas elements.

Recently, virtual element methods (VEM) for nonlinear (in-)elastic problems in the compressible and incompressible regime have been proposed [9, 7, 16, 48].

The linear TDNNS method introduced and analysed in [25, 27] does not suffer from shear locking or large aspect ratios [26]. Furthermore, volume locking in the nearly incompressible case can be avoided by adding a consistent stabilization term [45]. Therein, the displacement field is discretized by Nédélec elements resulting in less regularity requirements as for nodal elements. This, however, prevents the use of nonlinear material laws. Recently an Updated Lagrangian (UL) mixed scheme has been proposed for non-linear elasticity [28]. This mixed method is a two-field approach, where at convergence the independent fields are displacement and Cauchy stress.

In this work, we choose a different approach: we use the Hu–Washizu three-field principle. In the following, two different variants of three-field methods are deployed extending the (linear) TDNNS method. In the first variant, deformation gradient and first Piola–Kirchhoff stress are introduced as independent quantities. The independent deformation gradient may be interpreted as a lifting of the distributional gradient of the (discontinuous) displacement field. This method proved very robust in our numerical examples. In the second variant, Cauchy–Green strain and second Piola–Kirchhoff stress comprise the additional independent variables. In computations, rapid convergence of nonlinear iterations was observed. In a third approach, five independent fields are used: displacement, deformation gradient, Cauchy–Green strain, and first and second Piola–Kirchhoff stress. Mathematically, this five-field formulation corresponds to a lifting followed by a projection, trying to combine the advantages of the two three-field methods. The additional fields are discretized by a discontinuous version of so-called Regge elements; originally derived as geometric discretization of the Einstein field equation by Regge [36], further developed in [15], and given a finite element context through Christiansen [17]; enabling static condensation techniques. Therefore the final system involves only displacement and stress degrees of freedom making the methods computationally efficient.

This paper is organized as follows: in Section 1 notation of elasticity is introduced and Section 2 is devoted to summarize the linear TDNNS method. In Section 3 the three extensions of the TDNNS method to the large deformation regime are presented and an Updated Lagrangian scheme for these approaches is derived in Section 4. Finally, Section 5 describes the used finite element spaces in more detail and several numerical examples are presented, showing the excellent performance of the methods.

1 Large deformation elasticity

Let $\Omega \subset \mathbb{R}^d$ with $d = 2, 3$ denote the body of interest in (stress-free) reference configuration. We use reference coordinates $X \in \Omega$ to describe the position of a material point. Under deformation, material points X are mapped to spatial positions $x(X)$. The associated deformation field shall be denoted by u and is defined as

$$u : \Omega \rightarrow \mathbb{R}^d, \quad u(X) = x(X) - X. \quad (1.1)$$

In this work, all spatial derivatives are assumed to be with respect to X if not indicated otherwise. We use $\nabla = \nabla_X$, $\text{curl} = \text{curl}_X$ and $\text{div} = \text{div}_X$ defined in the standard ways. When applied to a second order tensor, the divergence operator is to be understood row-wise.

The deformation gradient \mathbf{F} is defined as

$$\mathbf{F} := \mathbf{I} + \nabla u. \quad (1.2)$$

We use $J := \det \mathbf{F}$ for the Jacobi determinant. Further, we introduce the (left) Cauchy–Green strain tensor \mathbf{C} and the Green strain tensor \mathbf{E} by

$$\mathbf{C} := \mathbf{F}^\top \mathbf{F}, \quad \mathbf{E} := \frac{1}{2} (\mathbf{C} - \mathbf{I}). \quad (1.3)$$

Throughout this work, we assume to be in a static regime without inertia forces. On a non-vanishing part Γ_D of the boundary, the displacement shall be prescribed such that $u = u_D$ on Γ_D . On the remaining part $\Gamma_N = \partial\Omega \setminus \Gamma_D$, surface tractions g are given. Moreover, the body of interest shall be subjected to an external volume load f . In an energy-based formulation, we need the work of external forces, which sums up to

$$W_{ext} = \int_{\Omega} f \cdot u \, dX + \int_{\Gamma_N} g \cdot u \, dS. \quad (1.4)$$

Let $\Psi(\cdot)$ be a hyperelastic potential, where we use the same symbol independently of which deformation measure \mathbf{F} , \mathbf{C} , or \mathbf{E} is used.

The (non-symmetric) first Piola–Kirchhoff stress is defined as the derivative

$$\mathbf{P} := \frac{\partial \Psi}{\partial \mathbf{F}}. \quad (1.5)$$

The symmetric second Piola–Kirchhoff stress tensor is related to Ψ and \mathbf{P} via

$$\mathbf{\Sigma} := 2 \frac{\partial \Psi}{\partial \mathbf{C}}, \quad \text{and} \quad \mathbf{F} \mathbf{\Sigma} = \mathbf{P}. \quad (1.6)$$

For the sake of completeness, we introduce the (symmetric) Cauchy stress tensor $\boldsymbol{\sigma}$, which is obtained transforming the first Piola–Kirchhoff stress to spatial configuration by the Piola transform,

$$\boldsymbol{\sigma} = \frac{1}{J} \mathbf{P} \mathbf{F}^\top. \quad (1.7)$$

The displacement field u satisfies the minimization problem

$$\int_{\Omega} \Psi(\mathbf{C}) \, dX - W_{ext} \rightarrow \min_{u \in V}, \quad (1.8)$$

where V denotes the set of all admissible displacement fields. We do not give a precise mathematical definition of the set V here, but only note that the condition “ $u = u_D$ on Γ_D ” is essential. Conditions on continuity and/or (weak) differentiability of $u \in V$ are detailed for the different finite element methods in Section 2 and Section 3.

Computing the first variation of (1.8) in direction δu yields the following variational equation, well known as *principle of virtual works*: Find $u \in V$ such that

$$\int_{\Omega} \mathbf{P} : \nabla \delta u \, dX = \int_{\Omega} f \cdot \delta u \, dX + \int_{\Gamma_N} g \cdot \delta u \, dS \quad \forall \delta u, \quad (1.9)$$

where $\delta u \in V_0$ lives in the set of admissible virtual displacements V_0 with $\delta u = 0$ on Γ_D . Integration by parts leads to the balance equation, which reads in strong form

$$-\operatorname{div}(\mathbf{P}) = f, \quad \mathbf{P}N = g \text{ on } \Gamma_N, \quad u = u_D \text{ on } \Gamma_D. \quad (1.10)$$

Above, N denotes the outer normal vector to $\partial\Omega$ in reference configuration.

A linear small-deformation model As it will be needed for theoretical considerations in the sequel, we shortly present the according linearized elasticity problem. Under the assumption of small deformations, material points X and spatial points x can be identified, leading to the linearized strain tensor

$$\varepsilon(u) := \frac{1}{2}(\nabla u + (\nabla u)^\top) \quad (1.11)$$

as a measure of the deformation. As the different stress tensors coincide in this case, we use $\boldsymbol{\sigma}$ for the stress in linearized elasticity. Assuming the potential Ψ to be quadratic in ε , the stress-strain relation is linear $\boldsymbol{\sigma} = \mathbb{D}\varepsilon(u)$, represented by the fourth order stiffness tensor \mathbb{D} . The principle of virtual works transforms from (1.9) to

$$\int_{\Omega} \mathbb{D}\varepsilon(u) : \varepsilon(\delta u) \, dX = \int_{\Omega} f \cdot \delta u \, dX + \int_{\Gamma_N} g \cdot \delta u \, dS. \quad (1.12)$$

Basic finite element ingredients To introduce any finite element method, let $\mathcal{T} = \{T\}$ be a regular finite element mesh of Ω . In the past, TDNNS elements for triangles, quadrilaterals, as well as tetrahedra, hexahedra and prismatic elements have been developed. The mesh \mathcal{T} may be a hybrid one, containing several of the aforementioned element types. For each element T we define its boundary ∂T and the corresponding outer normal vector N .

We introduce the following conventions for denoting normal and tangential components of vector and tensor fields: the normal component of a vector field v is denoted by $v_N := v \cdot N$, while the tangential component is given by $v_T := v - v_N N$. For a tensor field $\boldsymbol{\sigma}$, we introduce its normal vector $\sigma_N = \boldsymbol{\sigma}N$. This normal vector can again be split into a normal and tangential component, reading $\sigma_{NN} = (\boldsymbol{\sigma}N) \cdot N$ and $\sigma_{NT} = \boldsymbol{\sigma}N - \sigma_{NN}N$, respectively.

2 The linear TDNNS method

The tangential-displacement and normal-normal-stress (TDNNS) method introduced for linear elasticity in [25, 26, 27] uses mixed finite elements with tangential continuous displacement fields and normal-normal continuous stresses. These are also chosen as degrees of freedom (dofs).

We introduce the linear TDNNS method shortly; for details on the finite element spaces we refer to Section 5.

Assume u to be an admissible displacement finite element function, where by admissible we mean: u is piecewise smooth on \mathcal{T} , its tangential component u_T is continuous across element interfaces, and the tangential component satisfies the essential boundary condition on Γ_D , $u_T = (u_D)_T$. As the normal components are not necessarily continuous, gaps in normal direction may open up at

element interfaces, and need to be treated accordingly. As the stress is treated as an independent variable, admissible stress fields $\boldsymbol{\sigma}$ are introduced, where admissible means: $\boldsymbol{\sigma}$ is piecewise smooth symmetric on \mathcal{T} , its normal-normal component σ_{NN} is continuous across element interfaces, and it satisfies the boundary condition on Γ_N : $\sigma_{NN} = g_N$. The continuous normal component of the stress vector will control the displacement gaps.

Instead of the minimization problem (1.8), a saddle point problem for the Lagrangian is posed: find admissible displacement and stress fields minimizing respectively maximizing the Lagrangian

$$\mathcal{L}(u, \boldsymbol{\sigma}) := -\frac{1}{2} \int_{\Omega} \mathbb{D}^{-1} \boldsymbol{\sigma} : \boldsymbol{\sigma} dX + \langle \boldsymbol{\varepsilon}(u), \boldsymbol{\sigma} \rangle_{\mathcal{T}} - W_{ext}^{TDNNS} \rightarrow \min_u \max_{\boldsymbol{\sigma} \text{ adm.}}. \quad (2.1)$$

Note that the Lagrangian corresponds to the mechanic enthalpy of the system. The duality pairing $\langle \cdot, \cdot \rangle_{\mathcal{T}}$ is defined in the sense of distributions as neither the divergence of the stress nor the gradient of the displacement field is a globally regular function [25]

$$\begin{aligned} \langle \boldsymbol{\varepsilon}(u), \boldsymbol{\sigma} \rangle_{\mathcal{T}} &:= \sum_{T \in \mathcal{T}} \left(\int_T \boldsymbol{\sigma} : \nabla u dX - \int_{\partial T} \boldsymbol{\sigma}_{NN} u_N dS \right) \\ &= - \sum_{T \in \mathcal{T}} \left(\int_T \operatorname{div}(\boldsymbol{\sigma}) \cdot u dX - \int_{\partial T} \boldsymbol{\sigma}_{NT} \cdot u_T dS \right) = -\langle \operatorname{div}(\boldsymbol{\sigma}), u \rangle_{\mathcal{T}}. \end{aligned} \quad (2.2)$$

The work of external forces is adapted to read

$$W_{ext}^{TDNNS} = \int_{\Omega} f \cdot u dX + \int_{\Gamma_N} g_T \cdot u_T dS - \int_{\Gamma_D} (u_D)_N \sigma_{NN} dS. \quad (2.3)$$

After discretization, the above saddle point problem leads to a linear system of equations with an indefinite system matrix. However, a positive definite system matrix can be obtained using a *hybridization* technique. Therefore, the normal-normal continuity of the stresses is broken, such that σ_{NN} may be discontinuous across interfaces, and does not necessarily satisfy the stress boundary condition on Γ_N . A Lagrangian multiplier α is introduced, which enforces the lost continuity and boundary conditions. As, in the finite element scheme, both σ_{NN} and α are of the same polynomial order, the hybridized system is equivalent to the original one.

To be precise, let α be a vector-valued function defined on the skeleton \mathcal{E} , whose direction is normal to the interfaces. To be admissible, α shall moreover satisfy that $\alpha_N = (u_D)_N$ on the displacement boundary Γ_D . The hybridized TDNNS problem then reads

$$\begin{aligned} \mathcal{L}^h(u, \boldsymbol{\sigma}, \alpha) &:= \\ &- \frac{1}{2} \int_{\Omega} \mathbb{D}^{-1} \boldsymbol{\sigma} : \boldsymbol{\sigma} dX + \langle \boldsymbol{\varepsilon}(u), \boldsymbol{\sigma} \rangle_{\mathcal{T}} + \sum_{T \in \mathcal{T}} \int_{\partial T} \sigma_{NN} \alpha_N dS - W_{ext}^{TDNNSh} \rightarrow \min_u \min_{\alpha \text{ adm.}} \max_{\boldsymbol{\sigma} \text{ disc.}}, \end{aligned} \quad (2.4)$$

with the work of external forces

$$W_{ext}^{TDNNSh} = \int_{\Omega} f \cdot u dX + \int_{\Gamma_N} (g_T \cdot u_T + g_N \alpha_N) dS. \quad (2.5)$$

The additive term containing α indeed enforces normal-normal continuity of $\boldsymbol{\sigma}$, as can be seen by the following consideration: if the surface integrals are re-ordered facet by facet, there are two contributions to each internal facet with normal vectors N of opposite direction. Thus, $\alpha_N = \alpha \cdot N$ changes its sign, while σ_{NN} keeps its sign due to the quadratic occurrence of N . Considering boundary facets correctly, using N_E as a unique facet normal, and denoting the jump of the normal stress by $[\![\sigma_{N_E N_E}]\!]$, one observes

$$\sum_{T \in \mathcal{T}} \int_{\partial T} \sigma_{NN} \alpha_N dS = \sum_{E \in \mathcal{E}} \int_E [\![\sigma_{N_E N_E}]\!] \alpha_{N_E} dS, \quad (2.6)$$

where \mathcal{E} denotes the set of all interfaces, i.e., edges in two dimensions and faces in 3D.

It shows that the Lagrange multiplier α has the physical meaning of the normal component of the displacement [25]. As the discontinuous stress σ in (2.4) does not have any coupling dofs, one can use static condensation to eliminate it at element level, reducing the number of total dofs drastically for the final system, and making it therefore symmetric and positive definite (spd) again.

3 Nonlinear TDNNS

For nonlinear and thus, in general not explicitly invertible material laws the TDNNS methods (2.1) and (2.4) can not be applied. The main difficulty is that the gradient of the displacement field u is a distribution rather than a function. Therefore, multiplication might not be well defined, which is, however, crucial for handling nonlinear materials. In [28] recently an Updated Lagrangian scheme has been discussed to enable these sort of materials.

In this work, however, we will use the Hu–Washizu principle [47] introducing a new independent field. We will discuss three different approaches. In the first one we will lift $\nabla u + \mathbf{I}$ to the deformation gradient \mathbf{F} as a new unknown, which will be a regular function again. The second ansatz uses that for objective materials the energy potential Ψ depends on the Cauchy–Green strain tensor \mathbf{C} - or equivalently on the Green strain tensor \mathbf{E} - taking it as an additional field. The third approach combines the first two by first introducing a lifting to \mathbf{F} followed by a projection to \mathbf{C} , i.e., two additional fields are used.

In what follows, we will use the notation $\mathbf{F}(u) := \mathbf{I} + \nabla u$, $\mathbf{C}(u) := \mathbf{F}(u)^\top \mathbf{F}(u)$ and $\mathbf{E}(u) := 0.5(\mathbf{C}(u) - \mathbf{I})$ to indicate the dependence on the displacement, whereas \mathbf{F} , \mathbf{C} , and \mathbf{E} denote independent fields. Further, without restriction of generality but to simplify the problem at hand, we will use homogeneous traction forces $g = 0$ on Γ_N and homogeneous Dirichlet data $u_D = 0$ on Γ_D .

3.1 Lifting to \mathbf{F}

Instead of solving (1.8) one may define the following constrained minimization problem for piecewise smooth \tilde{u} on T , where \tilde{u} is continuous and satisfies the displacement boundary condition on Γ_D ,

$$\int_{\Omega} \Psi(\mathbf{F}) dX - W_{ext} \rightarrow \min_{\substack{\tilde{u} \text{ cont.} \\ \mathbf{F} = \mathbf{F}(\tilde{u})}}. \quad (3.1)$$

The corresponding Lagrange functional reads

$$\mathcal{L}(u, \mathbf{F}, \mathbf{P}) := \int_{\Omega} \Psi(\mathbf{F}) dX - W_{ext} - \int_{\Omega} (\mathbf{F} - \mathbf{I} - \nabla u) : \mathbf{P} dX, \quad (3.2)$$

with the first Piola–Kirchhoff stress tensor as Lagrange multiplier. For tangential-continuous displacement functions, however, the last integral in (3.2) is not well-defined, as ∇u does not exist in the sense of a square-integrable function. For normal-normal continuous (but non-symmetric) \mathbf{P} , the integral can be re-interpreted as a distribution. For u piecewise smooth tangential-continuous, \mathbf{P} piecewise smooth non-symmetric with P_{NN} continuous, and \mathbf{F} piecewise smooth discontinuous we obtain the saddle point problem

$$\mathcal{L}^{\mathbf{F}}(u, \mathbf{F}, \mathbf{P}) \rightarrow \min_u \max_{\mathbf{P} \text{ adm.}} \min_{\mathbf{F} \text{ disc.}}, \quad (3.3)$$

$$\text{with } \mathcal{L}^{\mathbf{F}}(u, \mathbf{F}, \mathbf{P}) := \int_{\Omega} \Psi(\mathbf{F}) dX - W_{ext}^{\text{TDNNS}} + \langle \nabla u, \mathbf{P} \rangle_{\mathcal{T}} - \int_{\Omega} (\mathbf{F} - \mathbf{I}) : \mathbf{P} dX \quad (3.4)$$

$$\text{and } \langle \nabla u, \mathbf{P} \rangle_{\mathcal{T}} = \sum_{T \in \mathcal{T}} \left(\int_T \nabla u : \mathbf{P} dX - \int_{\partial T} u_N P_{NN} dS \right). \quad (3.5)$$

Above, u_T and P_{NN} have to satisfy the corresponding boundary conditions on Γ_D and Γ_N , respectively. The work of external forces is adapted according to (2.3).

The three-field formulation (3.3) allows all kind of nonlinear material laws. As we use discontinuous elements for the additional deformation gradient field \mathbf{F} , it can be eliminated on element level, which makes the method competitive. Additionally, \mathbf{P} can be eliminated by hybridization. Therefore, as in the linear case, a vector field α in normal direction is added on all element interfaces. The first Piola–Kirchhoff stress is then assumed piecewise smooth but discontinuous, and the hybridized optimization problem reads for all u and α with $u_T = (u_D)_T$ and $\alpha_N = (u_D)_N$ on Γ_D :

$$\mathcal{L}_h^{\mathbf{F}}(u, \mathbf{F}, \mathbf{P}, \alpha) \rightarrow \min_{u \text{ adm.}} \min_{\alpha \text{ adm.}} \max_{\mathbf{P} \text{ disc.}} \min_{\mathbf{F} \text{ disc.}}, \quad (3.6)$$

$$\text{with } \mathcal{L}_h^{\mathbf{F}}(u, \mathbf{F}, \mathbf{P}, \alpha) := \mathcal{L}^{\mathbf{F}}(u, \mathbf{F}, \mathbf{P}) + \sum_{T \in \mathcal{T}} \int_{\partial T} P_{NN} \alpha_N dS, \quad (3.7)$$

where in the definition of $\mathcal{L}^{\mathbf{F}}$ the work of external forces W_{ext}^{TDNNS} is implicitly replaced by W_{ext}^{TDNNSh} given in (2.5).

After static condensation of \mathbf{F} and \mathbf{P} , a minimization problem in tangential-continuous u and normal-continuous α remains.

We note that the identity matrix \mathbf{I} can exactly be represented by the discontinuous elements used for \mathbf{F} . Thus, it is equivalent to use $\mathbf{G} := \mathbf{F} - \mathbf{I} = \nabla u$ as independent field instead of \mathbf{F} .

Gradient splitting However, we can further simplify (3.6)–(3.7) by using the additive splitting of the deformation gradient into a symmetric and a skew-symmetric part, $\mathbf{F} = \mathbf{F}_{\text{sym}} + \mathbf{F}_{\text{skw}}$. We note that the symmetric part \mathbf{F}_{sym} is related to the linearized strain tensor $\varepsilon(u)$, while the skew-symmetric part \mathbf{F}_{skw} is equivalent to $\text{curl}(u)$.

$$\mathbf{F}(u) = \mathbf{F}_{\text{sym}}(u) + \mathbf{F}_{\text{skw}}(u), \quad \mathbf{F}_{\text{sym}}(u) = \mathbf{I} + \varepsilon(u), \quad \mathbf{F}_{\text{skw}}(u) = \text{skw}(\text{curl}(u)), \quad (3.8)$$

with the skw-operator defined as

$$\text{skw}(v) := \frac{1}{2} \begin{pmatrix} 0 & -v \\ v & 0 \end{pmatrix} \text{ in 2D}, \quad \text{skw}(v) := \frac{1}{2} \begin{pmatrix} 0 & -v_3 & v_2 \\ v_3 & 0 & -v_1 \\ -v_2 & v_1 & 0 \end{pmatrix} \text{ in 3D}. \quad (3.9)$$

From theory for Maxwell’s equations (see e.g. the monograph by Monk [23]), it is well-known that for a piecewise smooth and tangentially continuous vector field, the curl-operator is well-defined in the sense of a square-integrable function. Thus, there is no need to “lift” the skew-symmetric part $\mathbf{F}_{\text{skw}}(u)$ to an independent \mathbf{F}_{skw} , as $\mathbf{F}_{\text{skw}}(u)$ is already in $L^2(\Omega)$. The (hybridized) Lagrangian from (3.7) can be adapted accordingly, now using only the symmetric part \mathbf{P}_{sym} of the first Piola–Kirchhoff stress as a multiplier for the constraint $\mathbf{F}_{\text{sym}} = \mathbf{F}_{\text{sym}}(u)$:

$$\mathcal{L}_h^{\mathbf{F}, \text{sym}}(u, \mathbf{F}_{\text{sym}}, \mathbf{P}_{\text{sym}}, \alpha) \rightarrow \min_{u \text{ adm.}} \min_{\alpha \text{ adm.}} \max_{\mathbf{P}_{\text{sym}} \text{ disc.}} \min_{\mathbf{F}_{\text{sym}} \text{ disc.}}, \quad (3.10)$$

$$\begin{aligned} \text{with } \mathcal{L}_h^{\mathbf{F}, \text{sym}}(u, \mathbf{F}_{\text{sym}}, \mathbf{P}_{\text{sym}}, \alpha) := & \int_{\Omega} \Psi(\mathbf{F}_{\text{sym}} + \text{skw}(\text{curl}(u))) dX - W_{ext}^{\text{TDNNSh}} \\ & + \langle \varepsilon(u), \mathbf{P}_{\text{sym}} \rangle_{\mathcal{T}} - \int_{\Omega} (\mathbf{F}_{\text{sym}} - \mathbf{I}) : \mathbf{P}_{\text{sym}} dX \\ & + \sum_{T \in \mathcal{T}} \int_{\partial T} P_{\text{sym}, NN} \alpha_N dS. \end{aligned} \quad (3.11)$$

Note that the normal-normal continuity condition for the first Piola–Kirchhoff stress is equivalent to the continuity of the normal-normal component of its symmetric part, as

$$P_{NN} = P_{\text{sym}, NN} \quad \text{and} \quad P_{\text{skw}, NN} = 0. \quad (3.12)$$

In the definition of the Lagrangian (3.11), we re-use the distributional definition of the duality pairing $\langle \varepsilon(\cdot), \cdot \rangle_{\mathcal{T}}$ from the linear TDNNS method in (2.2). Stress elements for the linear case can be used for the discretization of \mathbf{P}_{sym} . Further details on the choices of finite elements, also for the symmetric deformation gradient \mathbf{F}_{sym} , are provided in Section 5. This simplification leads to fewer local degrees of freedom than the original hybridized equation (3.6)–(3.7). One may recover \mathbf{P}_{skw} in a post-processing step by the equation $\frac{\partial \Psi}{\partial \text{skw}(\text{curl}(u))} = \mathbf{P}_{\text{skw}}$.

3.2 Lifting to \mathbf{C}

For objective materials the energy potential Ψ depends on the Cauchy–Green strain tensor \mathbf{C} . Thus, instead of solving the constrained minimization problem (3.1) we can postulate for a piecewise smooth and globally continuous \tilde{u} , satisfying $\tilde{u} = u_D$ on Γ_D , the problem

$$\int_{\Omega} \Psi(\mathbf{C}) dX - W_{\text{ext}} \rightarrow \min_{\substack{\tilde{u} \text{ cont.} \\ \mathbf{C} = \mathbf{C}(\tilde{u})}}, \quad (3.13)$$

with the corresponding Lagrangian

$$\mathcal{L}(u, \mathbf{C}, \boldsymbol{\Sigma}) := \int_{\Omega} \Psi(\mathbf{C}) dX - W_{\text{ext}} - \int_{\Omega} \frac{1}{2} \left(\mathbf{C} - \underbrace{(\nabla u + \mathbf{I})^{\top} (\nabla u + \mathbf{I})}_{=\mathbf{C}(u)} \right) : \boldsymbol{\Sigma} dX. \quad (3.14)$$

Here, the Lagrange multiplier $\boldsymbol{\Sigma}$ is given by the second Piola–Kirchhoff stress tensor, which can be readily seen by taking the first variation of (3.14) in direction $\delta \mathbf{C}$ together with (1.6)

$$\int_{\Omega} \frac{\partial \Psi}{\partial \mathbf{C}}(\mathbf{C}) : \delta \mathbf{C} - \frac{1}{2} \boldsymbol{\Sigma} : \delta \mathbf{C} dX = 0 \quad \forall \delta \mathbf{C}. \quad (3.15)$$

As discussed in Subsection 3.1 the integral in (3.14) is not well defined for tangential-continuous displacement fields. Further, the balance equation (1.10) implies that the first Piola–Kirchhoff tensor has to be normal-continuous rather than $\boldsymbol{\Sigma}$. Motivated by this, the second Piola–Kirchhoff stress tensor $\boldsymbol{\Sigma}$ and the Cauchy–Green strain tensor \mathbf{C} are assumed to be piecewise smooth discontinuous and the hybridization variable α is used to enforce the normal-normal continuity of $\mathbf{P} = \mathbf{F}\boldsymbol{\Sigma}$ yielding the following saddle point problem

$$\mathcal{L}_h^{\mathbf{C}}(u, \mathbf{C}, \boldsymbol{\Sigma}, \alpha) \rightarrow \min_{u \text{ adm.}} \min_{\alpha \text{ adm.}} \max_{\boldsymbol{\Sigma} \text{ disc.}} \min_{\mathbf{C} \text{ disc.}}, \quad (3.16)$$

$$\begin{aligned} \text{with } \mathcal{L}_h^{\mathbf{C}}(u, \mathbf{C}, \boldsymbol{\Sigma}, \alpha) := & \int_{\Omega} \Psi(\mathbf{C}) dX - W_{\text{ext}}^{\text{TDNNSh}} + \frac{1}{2} \langle \mathbf{C}(u), \boldsymbol{\Sigma} \rangle_{\mathcal{T}} - \frac{1}{2} \int_{\Omega} \mathbf{C} : \boldsymbol{\Sigma} dX \\ & + \sum_{T \in \mathcal{T}} \int_{\partial T} (\mathbf{F}(u)\boldsymbol{\Sigma})_{NN} \alpha_N dS \end{aligned} \quad (3.17)$$

$$\text{and } \langle \mathbf{C}(u), \boldsymbol{\Sigma} \rangle_{\mathcal{T}} := \sum_{T \in \mathcal{T}} \left(\int_T \mathbf{C}(u) : \boldsymbol{\Sigma} dX - 2 \int_{\partial T} u_N (\mathbf{F}(u)\boldsymbol{\Sigma})_{NN} dS \right). \quad (3.18)$$

The proof that this method is consistent, i.e., the smooth exact solution \tilde{u} of (1.10) together with $\alpha := \tilde{u}_N N$, $\mathbf{C} := \mathbf{C}(\tilde{u})$, and $\boldsymbol{\Sigma} := 2 \frac{\partial \Psi}{\partial \mathbf{C}}(\mathbf{C}(\tilde{u}))$ solves (3.16) can be found in Appendix A.

Again, due to the discontinuity of $\boldsymbol{\Sigma}$ and \mathbf{C} , they can be eliminated at element level and the resulting system involving u and α is positive. Therefore, the same amount of coupling dofs are needed as for the lifting of \mathbf{F} in the previous subsection.

Linearizing (3.17), see Appendix B, yields that in the small deformation regime (3.6) and (3.17) coincide. Further, assuming a quadratic potential Ψ the hybridized TDNNS method (2.4) can be recovered.

We note that due to the affine relation $\mathbf{E} = 0.5(\mathbf{C} - \mathbf{I})$ and

$$\frac{\partial \Psi}{\partial \mathbf{E}} : \delta \mathbf{E} = \frac{\partial \Psi}{\partial \mathbf{C}} : \delta \mathbf{C} \quad (3.19)$$

the problem

$$\int_{\Omega} \Psi(\mathbf{E}) dX - W_{ext} \rightarrow \min_{\substack{\tilde{u} \text{ cont.} \\ \mathbf{E}=\mathbf{E}(\tilde{u})}} \quad (3.20)$$

is equivalent to (3.13) and thus, one could use \mathbf{E} instead of \mathbf{C} as additional field.

Stabilization techniques To improve robustness of this method in the large deformation regime, one may add the following well known stabilization term

$$\sum_{T \in \mathcal{T}} \int_{\partial T} \frac{c_1}{h} (u - \alpha)_N (u - \alpha)_N dS \quad (3.21)$$

from Hybrid Discontinuous Galerkin (HDG) techniques [10, 18] to (3.17). Here, h denotes the ratio of the element volume and the boundary area, $h = \frac{J}{J_{\text{bnd}}}$ (J and J_{bnd} are the volume and area measures of the mapping from the reference to the physical element) used especially for anisotropic elements and $c_1 > 0$ is a positive constant. As there holds for the true solution $\tilde{u}_N = \alpha_N$, (3.21) is consistent.

A second stabilization technique consists of adding the consistent term

$$c_2 \sum_{T \in \mathcal{T}} \int_T (\mathbf{C} - \mathbf{C}(u)) : (\mathbf{C} - \mathbf{C}(u)) dX \quad (3.22)$$

enforcing the element-wise equality of the lifting with $c_2 > 0$. Note, that these terms increase the stability but lead to less accurate solutions if the stability parameters c_1 and c_2 are chosen too large.

3.3 Lifting to \mathbf{F} and projection to \mathbf{C}

In numerical experiments we observed that the method presented in Subsection 3.1, where a lifting of \mathbf{F} is considered, is more robust compared to the approach in the previous subsection, which may lead to more accurate solutions. The number of Newton iterations needed for one load step to converge, however, is significantly higher than for the second method. This motivates to combine both, leading to a lifting of \mathbf{F} , like in the first method. Then, the corresponding Cauchy–Green strain tensor $\mathbf{C}(\mathbf{F}) = \mathbf{F}^\top \mathbf{F}$ is going to be interpolated to an independent new field \mathbf{C} . This can be interpreted as a projection of $\mathbf{C}(\mathbf{F})$ to \mathbf{C} and thus, differs compared to the second approach, where \mathbf{C} is a lifting rather than a projection.

Again, we start with a constraint minimization problem for a piecewise smooth, globally continuous and admissible \tilde{u}

$$\int_{\Omega} \Psi(\mathbf{C}) dX - W_{ext} \rightarrow \min_{\substack{\tilde{u} \text{ cont.} \\ \mathbf{F}=\mathbf{F}(\tilde{u}) \\ \mathbf{C}=\mathbf{C}(\mathbf{F})}} \quad (3.23)$$

together with the Lagrangian

$$\mathcal{L}(u, \mathbf{F}, \mathbf{P}, \mathbf{C}, \boldsymbol{\Sigma}) := \int_{\Omega} \Psi(\mathbf{C}) dX - W_{ext} - \int_{\Omega} (\mathbf{F} - \nabla u - \mathbf{I}) : \mathbf{P} dX - \int_{\Omega} \frac{1}{2} (\mathbf{C} - \mathbf{F}^\top \mathbf{F}) : \boldsymbol{\Sigma} dX. \quad (3.24)$$

Computing the variation in direction $\delta \mathbf{C}$ yields like in the previous subsection that the Lagrange multiplier $\boldsymbol{\Sigma}$ is the second Piola–Kirchhoff stress tensor. With the variation in direction $\delta \mathbf{F}$ we obtain that \mathbf{P} corresponds to the first Piola–Kirchhoff stress tensor

$$\int_{\Omega} \mathbf{P} : \delta \mathbf{F} - \mathbf{F} \boldsymbol{\Sigma} : \delta \mathbf{F} dX = 0 \quad \forall \delta \mathbf{F}. \quad (3.25)$$

The integral involving the gradient of u in (3.24) is interpreted as a distribution as in Subsection 3.1 for piecewise smooth and tangential-continuous displacement fields. Together with \mathbf{P} piecewise smooth, non-symmetric and P_{NN} continuous, and \mathbf{F} , Σ and \mathbf{C} piecewise smooth discontinuous we postulate the following saddle point problem

$$\mathcal{L}^{\mathbf{FC}}(u, \mathbf{F}, \mathbf{P}, \mathbf{C}, \Sigma) \rightarrow \min_{u \text{ adm.}} \max_{\mathbf{P} \text{ adm.}} \min_{\mathbf{F} \text{ disc.}} \min_{\mathbf{C} \text{ disc.}} \max_{\Sigma \text{ disc.}}, \quad (3.26)$$

$$\text{with } \mathcal{L}^{\mathbf{FC}}(u, \mathbf{F}, \mathbf{P}, \mathbf{C}, \Sigma) := \int_{\Omega} \Psi(\mathbf{C}) dX - W_{ext}^{\text{TDNNS}} - \langle \mathbf{F} - \nabla u - \mathbf{I}, \mathbf{P} \rangle_{\mathcal{T}} - \int_{\Omega} \frac{1}{2} (\mathbf{C} - \mathbf{F}^{\top} \mathbf{F}) : \Sigma dX, \quad (3.27)$$

where $\langle \cdot, \cdot \rangle_{\mathcal{T}}$ is defined as in (3.5).

One may pose the hybridized Lagrangian $\mathcal{L}_h^{\mathbf{FC}}(u, \mathbf{F}, \mathbf{P}, \mathbf{C}, \Sigma, \alpha)$ according to (3.6)–(3.7). Further, in analogy to Subsection 3.1 the gradient splitting can be used to eliminate the skew-symmetric part of \mathbf{F} and \mathbf{P} yielding the Lagrangian $\mathcal{L}_h^{\mathbf{FC}, \text{sym}}(u, \mathbf{F}_{\text{sym}}, \mathbf{P}_{\text{sym}}, \mathbf{C}, \Sigma, \alpha)$.

The additional term

$$\int_{\Omega} (\mathbf{C} - \mathbf{F}^{\top} \mathbf{F}) : \Sigma dX \quad (3.28)$$

is well defined for piecewise smooth, discontinuous and thus, square-integrable functions. As a result \mathbf{C} is the (local) L^2 -projection of $\mathbf{F}^{\top} \mathbf{F}$ onto the space of polynomial order k used for Σ , see Section 5,

$$\mathbf{C} = \mathcal{I}_{L^2}^k(\mathbf{F}^{\top} \mathbf{F}). \quad (3.29)$$

We note that this method is equivalent to the first approach if the polynomial order for \mathbf{C} and Σ are chosen large enough, namely twice as the degree used for \mathbf{F} . Further, in the small strain regime $\mathcal{L}_h^{\mathbf{FC}}(u, \mathbf{F}, \mathbf{P}, \mathbf{C}, \Sigma, \alpha)$ reduces also to the hybridized linear TDNNS method (2.4), as (3.28) becomes

$$\int_{\Omega} (\mathbf{C} - \mathbf{I} + \varepsilon(u)) : \Sigma dX. \quad (3.30)$$

For this method Σ , \mathbf{P} , \mathbf{C} , and \mathbf{F} can be eliminated by static condensation techniques at element level leading to a minimization problem in u and α . Thus, the number of coupling dofs coincide with those in Subsections 3.1 and 3.2. However, the number of local dofs is higher compared to the previous methods.

4 Updated Lagrangian

In problems with large rotations, normal and tangential directions vary strongly when going from reference to actual configuration. This may lead to problems – for the methods with lifting to \mathbf{F} or \mathbf{F}/\mathbf{C} , we observed less than optimal behavior for thin structured elements, while for the method with lifting to \mathbf{C} even breakdown was observed as the rotations approached 90° . To alleviate these problems, we propose to use an Updated Lagrangian scheme, where in each load step the configuration obtained in the last load step is used as intermediate configuration. As one may assume rotations within a single load step to be less than 90° , better behavior of the method is expected.

To describe the Updated Lagrangian based method, we follow [28] and introduce the notion of an *intermediate configuration*. Starting from reference configuration Ω , the deformation $X \rightarrow x = X + u(X)$ associated to the displacement field u maps Ω to the spatial configuration $\omega \subset \mathbb{R}^d$. In the following we introduce a multiplicative splitting of the deformation, introducing some “intermediate” displacement u_0 and a “displacement update” u_Δ ,

$$u(X) = u_0(X) + u_\Delta(x_0(X)) \quad \text{with} \quad x_0(X) = X + u_0(X). \quad (4.1)$$

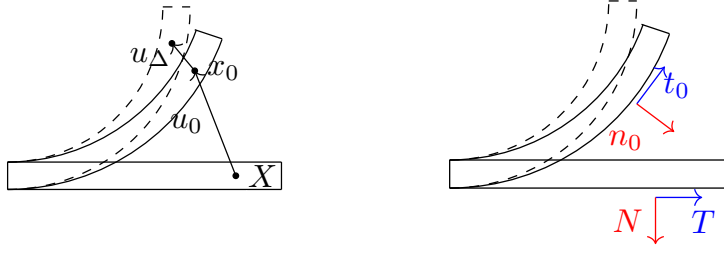


Figure 4.1: Reference configuration, intermediate configuration and actual configuration.

While the intermediate displacement u_0 is known and fixed in each load step, the displacement update u_Δ is the unknown quantity to be computed. The according configuration $\omega_0 := x_0(\Omega)$ shall be referred to as intermediate configuration. Boundary parts Γ_D and Γ_N are transformed to $\gamma_{D,0}$ and $\gamma_{N,0}$, respectively. For a graphical visualization of the different configurations see Figure 4.1. One easily verifies the multiplicative splitting of the deformation gradient \mathbf{F} ,

$$\mathbf{F}(u) = \mathbf{F}_\Delta(u_\Delta)\mathbf{F}_0(u_0) \quad (4.2)$$

with

$$\mathbf{F}_0 = \mathbf{F}_0(u_0) = \mathbf{I} + \nabla_X u_0, \quad \mathbf{F}_\Delta(u_\Delta) = \mathbf{I} + \nabla_{x_0} u_\Delta. \quad (4.3)$$

Above and in the following we will omit writing the explicit dependence of \mathbf{F}_0 on u_0 , as \mathbf{F}_0 will not be used as an independent unknown. For the update gradient $\mathbf{F}_\Delta(u_\Delta)$ we explicitly state the dependence in all occurrences, to distinguish the gradient from the independent \mathbf{F}_Δ introduced in the lifting procedure later.

The triangulation \mathcal{T} of Ω is mapped to a – possibly curved – triangulation \mathcal{T}_0 of ω_0 . The unit outward normal vector N in reference configuration is transformed to n_0 with respect to the intermediate configuration following

$$n_0 = \frac{J_0}{J_{\text{bnd},0}} \mathbf{F}_0^{-\top} N \quad \text{with} \quad J_0 = \det \mathbf{F}_0, \quad J_{\text{bnd},0} = J_0 \|\mathbf{F}_0^{-\top} N\|_2. \quad (4.4)$$

Note that in the definition above, $J_{A,0}$ denotes the transformation of the area element with normal N , while J_0 is the transformation of the volume element. Normal and tangential components of vector or tensor fields are then defined using the transformed normal n_0 and denoted by subscripts n_0 and t_0 , respectively.

Using the correct transformation rules, the deformation measures \mathbf{C} and J can be decomposed. To this end, let $\mathbf{C}_\Delta(u_\Delta) = (\mathbf{F}_\Delta(u_\Delta))^\top \mathbf{F}_\Delta(u_\Delta)$ be the Cauchy-Green tensor associated to u_Δ acting on ω_0 . By $J_\Delta(u_\Delta) = \det(\mathbf{F}_\Delta(u_\Delta))$ we mean the according Jacobi determinant. They are connected to their absolute counterparts $\mathbf{C}(u)$ and $J(u)$ via

$$\mathbf{C}(u) = \mathbf{F}_0^\top \mathbf{C}_\Delta(u_\Delta) \mathbf{F}_0, \quad J(u) = J_0 J_\Delta(u_\Delta). \quad (4.5)$$

As mentioned before, the intermediate configuration ω_0 and the according displacement part u_0 is assumed known and constant in each load step. The displacement update u_Δ on the other hand is a-priori unknown and a finite element solution shall be found. In this setting, the additional kinematic unknowns to be introduced will be independent \mathbf{F}_Δ and \mathbf{C}_Δ rather than \mathbf{F} or \mathbf{C} .

The internal energy, which appears in all formulations, can then be re-written after a transformation of the volume integral using the independent \mathbf{F}_Δ or \mathbf{C}_Δ

$$\int_\Omega \Psi(\mathbf{F}) dX = \int_{\omega_0} J_0^{-1} \Psi(\mathbf{F}_\Delta \mathbf{F}_0) dx_0, \quad (4.6)$$

$$\int_\Omega \Psi(\mathbf{C}) dX = \int_{\omega_0} J_0^{-1} \Psi(\mathbf{F}_0^\top \mathbf{C}_\Delta \mathbf{F}_0) dx_0. \quad (4.7)$$

4.1 Lifting to \mathbf{F}_Δ

For a moment, assume the displacement function weakly differentiable, $u_\Delta \in [H^1(\omega_0)]^d$. The correct Lagrange functional corresponding to (3.2) using the intermediate configuration and multiplicative decomposition of displacements reads

$$\mathcal{L}(u_\Delta, \mathbf{F}_\Delta, \mathbf{P}_0) := \int_{\omega_0} J_0^{-1} \Psi(\mathbf{F}_\Delta \mathbf{F}_0) dx_0 - W_{ext,0} - \int_{\omega_0} (\mathbf{F}_\Delta - \mathbf{I} - \nabla_{x_0} u_\Delta) : \mathbf{P}_0 dx_0, \quad (4.8)$$

with the work of external forces

$$W_{ext,0} = \int_{\omega_0} J_0^{-1} f \cdot u_\Delta dx_0 + \int_{\gamma_{N,0}} J_{\text{bnd},0}^{-1} g \cdot u_\Delta ds_0. \quad (4.9)$$

One easily verifies that the Lagrangian multiplier \mathbf{P}_0 is connected to the Piola-Kirchhoff stress \mathbf{P} via

$$\mathbf{P}_0 = J_0^{-1} \mathbf{P} \mathbf{F}_0^\top. \quad (4.10)$$

As in Subsection 3.1, we can now derive a (hybridized) TDNNS method in intermediate configuration. For u_Δ piecewise smooth and tangential-continuous on the triangulation \mathcal{T}_0 of ω_0 , \mathbf{P}_0 piecewise smooth non-symmetric with $(P_0)_{n_0 n_0}$ continuous, and \mathbf{F}_Δ piecewise discontinuous we obtain a saddle point problem similar to (3.3)–(3.5),

$$\mathcal{L}_0^{\mathbf{F}}(u_\Delta, \mathbf{F}_\Delta, \mathbf{P}_0) \rightarrow \min_{u_\Delta \text{ adm.}} \max_{\mathbf{P}_0 \text{ adm.}} \min_{\mathbf{F}_\Delta \text{ adm.}}, \quad (4.11)$$

$$\begin{aligned} \text{with } \mathcal{L}_0^{\mathbf{F}}(u_\Delta, \mathbf{F}_\Delta, \mathbf{P}_0) &:= \int_{\omega_0} J_0^{-1} \Psi(\mathbf{F}_\Delta \mathbf{F}_0) dx_0 - W_{ext,0} \\ &+ \langle \nabla_{x_0} u_\Delta, \mathbf{P}_0 \rangle_{\mathcal{T}_0} - \int_{\omega_0} (\mathbf{F}_\Delta - \mathbf{I}) : \mathbf{P}_0 dx_0, \end{aligned} \quad (4.12)$$

$$\begin{aligned} W_{ext,0}^{\text{TDNNS}} &= \int_{\omega_0} J_0^{-1} f \cdot u_\Delta dx_0 + \int_{\gamma_{N,0}} J_{\text{bnd},0}^{-1} g_{t_0} \cdot (u_\Delta)_{t_0} ds_0 \\ &- \int_{\gamma_{D,0}} (u_D - u_0)_{n_0} (P_0)_{n_0 n_0} ds_0, \end{aligned} \quad (4.13)$$

$$\text{and } \langle \nabla_{x_0} u_\Delta, \mathbf{P}_0 \rangle_{\mathcal{T}_0} = \sum_{T_0 \in \mathcal{T}_0} \left(\int_{T_0} \nabla_{x_0} u_\Delta : \mathbf{P}_0 dx_0 - \int_{\partial T_0} (u_\Delta)_{n_0} (P_0)_{n_0 n_0} ds_0 \right). \quad (4.14)$$

Additionally, in (4.11)–(4.14) the following boundary conditions have to be satisfied for u_Δ and \mathbf{P}_0 to be admissible,

$$(u_\Delta)_{t_0} = (u_D - u_0)_{t_0} \quad \text{and} \quad (P_0)_{n_0 n_0} = J_{A,0}^{-1} g_{n_0}. \quad (4.15)$$

As in (3.6)–(3.7) hybridization is again possible in order to regain a symmetric positive system. The hybridized problem reads for all u_Δ and \mathbf{F}_Δ as above, \mathbf{P}_0 piecewise smooth discontinuous not necessarily satisfying the boundary condition from (4.15), and n_0 -continuous Lagrangian multipliers α on element interfaces with $\alpha_{n_0} = (u_D - u_0)_{n_0}$ on $\gamma_{D,0}$:

$$(u_\Delta, \mathbf{F}_\Delta, \mathbf{P}_0, \alpha) \rightarrow \min_{u_\Delta \text{ adm.}} \min_{\alpha \text{ adm.}} \max_{\mathbf{P}_0 \text{ disc.}} \min_{\mathbf{F}_\Delta \text{ adm.}}, \quad (4.16)$$

$$\text{with } \mathcal{L}_{0,h}^{\mathbf{F}} := \mathcal{L}_0^{\mathbf{F}}(u_\Delta, \mathbf{F}_\Delta, \mathbf{P}_0) + \sum_{T_0 \in \mathcal{T}_0} \int_{\partial T_0} (P_0)_{n_0 n_0} \alpha_{n_0} ds_0, \quad (4.17)$$

in which $W_{ext,0}^{\text{TDNNS}}$ is replaced by

$$W_{ext,0}^{\text{TDNNSh}} := \int_{\omega_0} J_0^{-1} f \cdot u_\Delta dx_0 + \int_{\gamma_{N,0}} J_{\text{bnd},0}^{-1} (g_{t_0} \cdot (u_\Delta)_{t_0} + g_{n_0} \alpha_{n_0}) ds_0. \quad (4.18)$$

4.2 Lifting to \mathbf{C}_Δ or lifting to \mathbf{F}_Δ with projection to \mathbf{C}_Δ

The variants described in Subsection 3.2 as well as Subsection 3.3 are transformed to the Updated Lagrangian setting in the same way. The update tensors \mathbf{C}_Δ and, in latter case, also \mathbf{F}_Δ are discretized independently.

5 Numerics

5.1 Finite element spaces

For the sake of simplicity of presentation, we assume \mathcal{T} to be a simplicial triangulation. Note, however, that hybrid meshes can directly be treated using different elements in the same mesh. On the triangulation \mathcal{T} we define the set of all piecewise polynomials up to order k by $\Pi^k(\mathcal{T})$ and the polynomials living only on the skeleton \mathcal{E} are denoted by $\Pi^k(\mathcal{E})$.

We define the following finite element spaces of order k

$$V^k := \{v \in [\Pi^k(\mathcal{T})]^d : v \text{ continuous}\}, \quad (5.1a)$$

$$U^k := \{u \in [\Pi^k(\mathcal{T})]^d : u_T \text{ continuous}\}, \quad (5.1b)$$

$$\Gamma^k := \{\alpha \in [\Pi^k(\mathcal{E})]^d : \alpha_N \text{ continuous}\}, \quad (5.1c)$$

$$\Sigma^k := \{\sigma \in [\Pi^k(\mathcal{T})]_{\text{sym}}^{d \times d} : \sigma_{NN} \text{ continuous}\}, \quad (5.1d)$$

$$\mathcal{R}^k := \{\mathbf{C} \in [\Pi^k(\mathcal{T})]_{\text{sym}}^{d \times d} : \mathbf{C}_{TT} \text{ continuous}\}. \quad (5.1e)$$

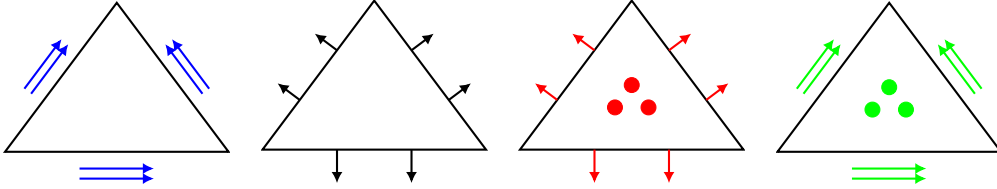


Figure 5.1: Nédélec, hybridization, stress and Regge finite element for $k = 1$.

The set of all piecewise polynomials which are globally continuous is denoted by V and corresponds to the well known Lagrangian nodal finite elements [51]. The space U is given by the Nédélec elements, where the vector valued polynomials are tangential continuous over elements [24]. The hybridization space Γ can be implemented by using a facet space equipped with the normal vector [10]. As it follows the same transformation rules as H(div)-conforming Raviart–Thomas (RT) [30] or Brezzi–Douglas–Marini (BDM) [14] elements, they can also be used (neglecting their inner dofs). The stress space Σ consists of the normal-normal continuous elements introduced in [25]. For two-dimensional domains, triangular and quadrilateral elements have been introduced, while for three-dimensional meshes tetrahedra, hexahedra and prismatic elements have been developed so far, see [25, 26, 22]. The so-called Regge finite element space is constructed such that the tangential-tangential part $\mathbf{C}_{TT} := (\mathbf{I} - \mathbf{N} \otimes \mathbf{N})\mathbf{C}(\mathbf{I} - \mathbf{N} \otimes \mathbf{N})$, one component in 2D and four in 3D, is continuous. Here \otimes denotes the dyadic product of two vectors. For a construction of Regge elements for triangles and tetrahedra we refer to [21]. The construction of arbitrary order quadrilateral, prismatic, and hexahedra Regge elements is topic of an upcoming paper. Constructions based on hierarchical elements for the spaces (5.1a)–(5.1c) are given e.g. in [50]. In Figure 5.1 triangular finite elements of (5.1b)–(5.1e) of polynomial order $k = 1$ are depicted.

One may break the continuity of the spaces Σ^k and \mathcal{R}^k for the presented methods, which will be denoted by $\Sigma^{k,*}$ and $\mathcal{R}^{k,*}$, respectively. Therefore, the same basis as for the continuous spaces are used, but no continuity over interfaces is required, i.e., the corresponding functions are discontinuous.

For the lifting of \mathbf{F} method in Subsection 3.1 the tangential-continuous displacement field u will be discretized with Nédélec elements $u \in U^k$, whereas for the normal-continuous hybridization variable α the space Γ^k is used. For the Lagrangian $\mathcal{L}_h^{\mathbf{F}, \text{sym}}(u, \mathbf{F}_{\text{sym}}, \mathbf{P}_{\text{sym}}, \alpha)$ given in (3.11) the (symmetric part of the) first Piola–Kirchhoff stress tensor \mathbf{P}_{sym} is discretized by the stress space $\Sigma^{k, \star}$ such that the duality product $\langle \varepsilon(u), \mathbf{P}_{\text{sym}} \rangle_{\mathcal{T}}$ is well defined [25]. Let us shortly motivate the choice of Regge-elements for the lifted deformation gradient \mathbf{F} : for the deformation gradient \mathbf{F} of a piecewise smooth and globally continuous displacement field \tilde{u} we observe that its gradient is tangential continuous, i.e., $\mathbf{F}_T := \mathbf{F}(\mathbf{I} - N \otimes N)$ is continuous. Taking the symmetric part of \mathbf{F} gives a tangential-tangential continuous field \mathbf{F}_{sym} , motivating to use the discontinuous Regge finite elements, $\mathbf{F}_{\text{sym}} \in \mathcal{R}^{k, \star}$. Further, the Nédélec elements transform covariantly. More precisely, for the reference element \hat{T} assume an affine transformation ϕ to a physical element, $\phi : \hat{T} \rightarrow T$, and define the corresponding gradient $\mathbf{G} = \nabla_{\hat{x}} \phi$. Let \hat{u} be a Nédélec element on the reference element \hat{T} . Then, with the definition $u \circ \phi = \mathbf{G}^{-\top} \hat{u}$, u is a Nédélec element on the physical element T , cf. [23]. The gradient of this tangential-continuous displacement field u transforms with $(\nabla_X u) \circ \phi = \mathbf{G}^{-\top} \nabla_{\hat{x}} \hat{u} \mathbf{G}^{-1}$, i.e., doubled covariantly. The tangential-tangential continuous Regge elements are constructed such that the mapping is also a double covariant transformation, $\mathbf{F} \circ \phi = \mathbf{G}^{-\top} \hat{\mathbf{F}} \mathbf{G}^{-1}$. Therefore, in $\int_{\Omega} (\mathbf{F} - \nabla u) : \mathbf{P} dX$ both, \mathbf{F} and ∇u , are transformed in the same manner from reference to affine-linear element. For non-affine transformations there holds (gradient of \mathbf{G} has to be interpreted in the correct way) $(\nabla_X u) \circ \phi = \nabla_{\hat{x}} (\mathbf{G}^{-\top} \hat{u}) \mathbf{G}^{-1} = \mathbf{G}^{-\top} (\nabla_{\hat{x}} \hat{u} - \nabla_{\hat{x}} \mathbf{G}^{\top} \mathbf{G}^{-\top} \hat{u}) \mathbf{G}^{-1}$ and thus transforms also doubled covariantly. Summing up, for the first method (3.11) we seek for $(u, \alpha, \mathbf{F}_{\text{sym}}, \mathbf{P}_{\text{sym}})$ in $U^k \times \Gamma^k \times \mathcal{R}^{k, \star} \times \Sigma^{k, \star}$.

The second approach uses the same spaces as the first one, we seek for $(u, \alpha, \mathbf{C}, \Sigma)$ in $U^k \times \Gamma^k \times \mathcal{R}^{k, \star} \times \Sigma^{k, \star}$. Again, for a continuous \tilde{u} it follows that \mathbf{F} is tangential-continuous and thus, $\mathbf{C} = \mathbf{F}^{\top} \mathbf{F}$ is tangential-tangential continuous.

For the third method the solution $(u, \alpha, \mathbf{F}_{\text{sym}}, \mathbf{P}_{\text{sym}}, \mathbf{C}, \Sigma)$ lives in $U^k \times \Gamma^k \times \mathcal{R}^{k, \star} \times \Sigma^{k, \star} \times \mathcal{R}^{k, \star} \times \mathcal{R}^{k, \star}$. The choices for $\mathbf{F}_{\text{sym}}, \mathbf{P}_{\text{sym}}, \mathbf{C}$ follow the same ideas as before. Motivated by the L^2 -interpolation term (3.28) the same space for Σ is used as for \mathbf{C} .

5.2 Examples

All methods are implemented in the open source finite element library Netgen/NGSolve¹ [37, 38]. In what follows we will denote the first, second, and third method as **F**-, **C**-, and **FC**-based method, respectively. We observed that the **F**-based method is more robust compared to the **C**-based method giving slightly better results, however more Newton iteration steps are needed for every load step. The **FC**-based method combines both advantages, the accuracy of **F**- and the faster Newton convergence of **C**-based method at the expense of being locally more expensive, due to the higher amount of local dofs.

For all benchmarks, if nothing stated otherwise, second order methods, $k = 2$ are used. We stress that also polynomial degree $k = 1$ can be used as well as higher polynomial orders. The methods are also compared with standard Lagrangian elements of polynomial order $k = 2$ for the displacement u denoted by method “std”. We note that for the same grids the coupling dofs of our methods are nearly doubled compare to the standard Lagrangian method in two dimensions as there are asymptotically more edges than vertices, namely $\#E \approx 3\#V$, where the dofs are placed (see Figure 5.1). In the three dimensional case the coupling type dofs are approximately four times due to the fact that $\#E \approx 7\#V$.

To solve the arising nonlinear problems a (damped) Newton method is used together with load steps to increase the right-hand side. As we started with (constraint) minimization problems the stiffness matrices appearing in the Newton iterations are symmetric. Further, due to the static condensation, the resulting (smaller) system is also a minimization problem, enabling the use of the built in *sparsecholesky* solver. Full code examples are available².

¹www.ngsolve.org

²www.gitlab.com/mneunteufel/nonlinear_elasticity

We will consider two different material laws of neo-Hooke as hyperelastic potentials, namely

$$\begin{cases} \Psi_1(\mathbf{F}) := \frac{1}{2} (\text{tr}(\mathbf{F}^\top \mathbf{F}) - d) - \mu \log \det \mathbf{F} + \frac{\lambda}{2} (\det \mathbf{F} - 1)^2, \\ \Psi_1(\mathbf{C}) := \frac{1}{2} (\text{tr}(\mathbf{C}) - d) - \frac{\mu}{2} \log \det \mathbf{C} + \frac{\lambda}{2} (\sqrt{\det \mathbf{C}} - 1)^2, \end{cases} \quad (5.2a)$$

$$\begin{cases} \Psi_2(\mathbf{F}) := \frac{1}{2} (\text{tr}(\mathbf{F}^\top \mathbf{F}) - d) - \mu \log \det \mathbf{F} + \frac{\lambda}{2} (\log \det \mathbf{F})^2, \\ \Psi_2(\mathbf{C}) := \frac{1}{2} (\text{tr}(\mathbf{C}) - d) - \frac{\mu}{2} \log \det \mathbf{C} + \frac{\lambda}{8} (\log \det \mathbf{C})^2, \end{cases} \quad (5.2b)$$

where μ and λ are the Lamé parameters and $d = 2, 3$ the spatial dimension.

5.2.1 Shearing Plate

A clamped square plate with length 1 mm is subjected to shear loads, see Figure 5.2. This benchmark has been considered in [1, 32]. We assume the displacement field

$$U_{ex} = \begin{pmatrix} \frac{1}{2}y^3 + \frac{1}{2}\sin\left(\frac{\pi y}{2}\right) \\ 0 \end{pmatrix}$$

and the neo-Hookean material law (5.2a) with parameters $\mu = \lambda = 1 \text{ N mm}^{-2}$ is used. With U_{ex} at hand the corresponding right hand sides f and g can be readily computed. Unstructured triangular meshes are used and in Figure 5.3 the final deformation is depicted. The results for all methods can be found in Table 5.1, and Figure 5.4 shows the error of the displacement $\|U - U_{ex}\|$ and deformation gradient $\|\mathbf{F} - \mathbf{F}_{ex}\|$. Note that for the \mathbf{C} -based method $\|\mathbf{C} - \mathbf{C}_{ex}\|$ is computed instead, as the approach does not use the deformation gradient \mathbf{F} . Thus, the corresponding error curve is shifted above compared to the others. We observe the expected optimal rates for all methods, cubic for the displacement U and quadratic for \mathbf{F} and \mathbf{C} , respectively. For the \mathbf{C} -based method, however, we needed stabilization (3.21) with $c_1 = 1$ to guarantee convergence for finer grids.

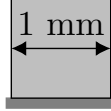


Figure 5.2: Geometry of shearing plate example.

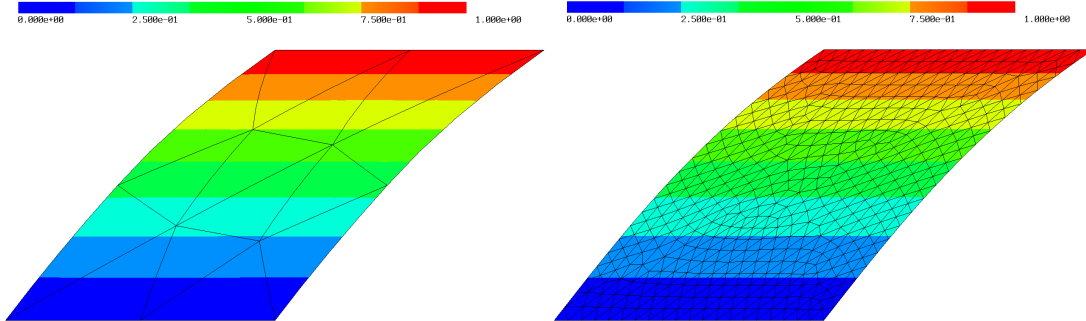


Figure 5.3: Final deformation of shearing plate example with 14 and 934 elements.

5.2.2 Cook's Membrane

We consider the Cook's membrane problem, see Figure 5.5, which has been used as a benchmark problem by [1, 32]. Material parameters for the hyperelastic potential (5.2b) are $\mu = 80.194 \text{ N mm}^{-2}$ and $\lambda = 40889.8 \text{ N mm}^{-2}$, which results in nearly incompressible behavior. The

	ne	dof	coupl. dof	$\ U - U_{ex}\ $	$\ \mathbf{F} - \mathbf{F}_{ex}\ $
F	14	852	138	4.11e-04	7.01e-03
	56	3390	534	5.86e-05	1.99e-03
	230	13860	2130	6.24e-06	4.53e-04
	938	56400	8562	6.64e-07	1.03e-04
	3724	223680	33756	8.22e-08	2.57e-05
C	14	852	138	5.12e-04	1.64e-02*
	56	3390	534	6.15e-05	4.63e-03*
	230	13860	2130	6.62e-06	1.08e-03*
	938	56400	8562	7.04e-07	2.50e-04*
	3724	223680	33756	8.70e-08	6.17e-05*
FC	14	1692	138	4.11e-04	7.01e-03
	56	6750	534	5.86e-05	1.99e-03
	230	27660	2130	6.24e-06	4.53e-04
	938	112680	8562	6.64e-07	1.03e-04
	3724	447120	33756	8.22e-08	2.57e-05

Table 5.1: Results for shearing plate example. For all methods the number of elements, number of dofs and coupling dofs, and the L^2 -error of the displacement and deformation gradient are presented. *: For the **C**-based method $\|\mathbf{C} - \mathbf{C}_{ex}\|_{L^2}$ is computed.

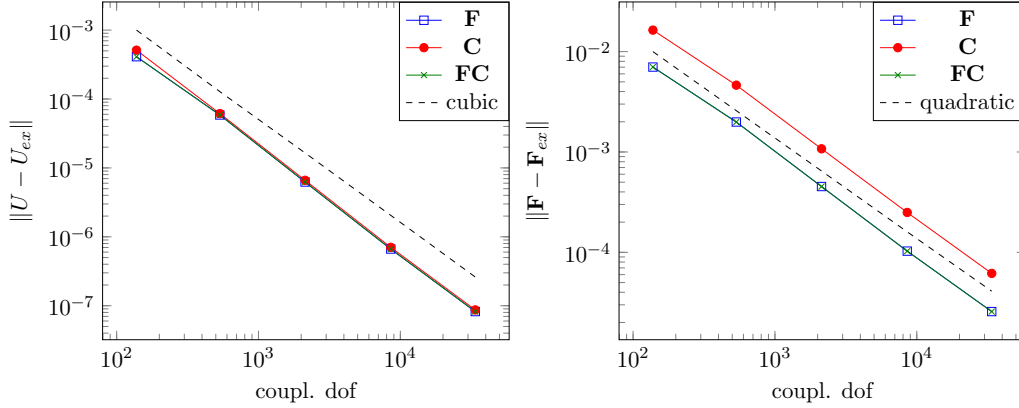


Figure 5.4: L^2 -errors of the methods with respect to the coupling dofs for shearing plate example. Left: displacement error $\|U - U_{ex}\|$. Right: error of deformation gradient $\|\mathbf{F} - \mathbf{F}_{ex}\|$ for **F**- and **FC**-based method and Cauchy–Green strain tensor $\|\mathbf{C} - \mathbf{C}_{ex}\|$ for **C**-based method.

quantity of interest is given by the vertical deflection at point *A*, cf. Figure 5.5. Different shear forces $f = 8, 16, 24, 32 \text{ N mm}^{-2}$ are considered and structured quadrilateral meshes with 2×2 , 4×4 , 8×8 , 16×16 , and 32×32 grids are used. It is well known that on the top left corner a singularity leads to reduced convergence rates. For this reason mostly adaptive (triangular) meshes are used to resolve the singularity. For the proposed methods, however, already a coarse 2×2 quadrilateral grid produces surprisingly accurate results being already in the correct magnitude, see Figure 5.6. In Figure 5.7 a comparison between the standard and **F**-based method for $f = 32$ is shown, where a clear difference in the vertical deflection can be seen. We observed that the quadrilateral on the top left deforms also on the clamped boundary, as the components are not prescribed point-wise giving the proposed methods more flexibility.

For the **C**-based method stabilization techniques (3.21) and (3.22) are used with parameters $c_1 = 1$ and $c_2 = \frac{\mu}{2}$, respectively. With them, only on the finest grid for the large forces $f = 24, 32$ Newton's method did not converge. The results for all forces can be found in Tables 5.2 – 5.3. All results agree with those in [1, 32].

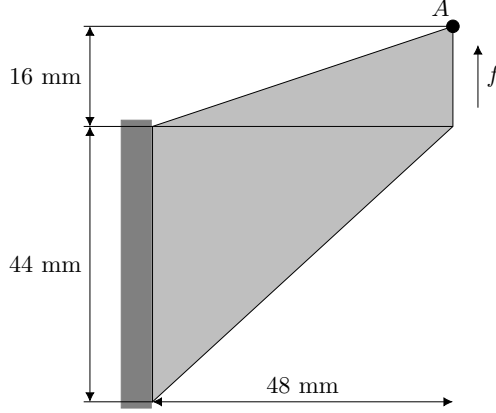


Figure 5.5: Geometry of Cook's membrane example.

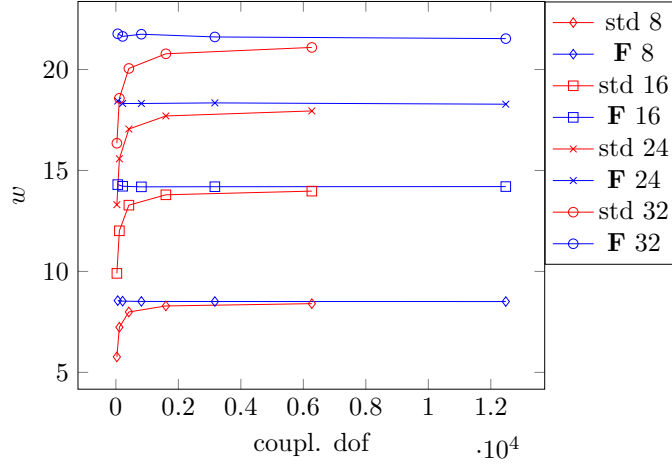


Figure 5.6: Vertical deflection w at point A for Cook's membrane example for $f = 8, 16, 24, 32$ with standard and **F**-based method.

5.2.3 Thin Beam

For the thin beam example we follow [32, 49], where the beam is clamped at the left side and a point load at A is applied. But instead of a point load we choose a shear force $f = 1 \text{ N mm}^{-2}$ on the right boundary such that the displacement is in the same magnitude, see Figure 5.8. This modification is needed as point-evaluation is not well defined in context of Sobolev spaces and traces, and cannot be set directly in terms of the TDNNS method. There, only the tangential trace is well defined for the displacement u and the normal trace for the hybridization variable α . The quantity of interest is again the vertical deflection at point A . Structured quadrilateral meshes with 10×1 , 20×2 , 40×4 , and 80×8 grids are used. The material parameters are $\mu = 6000 \text{ N mm}^{-2}$ and $\lambda = 24000 \text{ N mm}^{-2}$ and the hyperelastic potential (5.2b) is considered.

We observe that all three methods perform well, even for the coarsest grid. As discussed and shown in [26] the linear TDNNS method is extremely robust for anisotropic elements. The standard Lagrangian method converges also, however, it needs a finer grid to produce accurate solutions, see Table 5.4 and Figure 5.9 for the results.

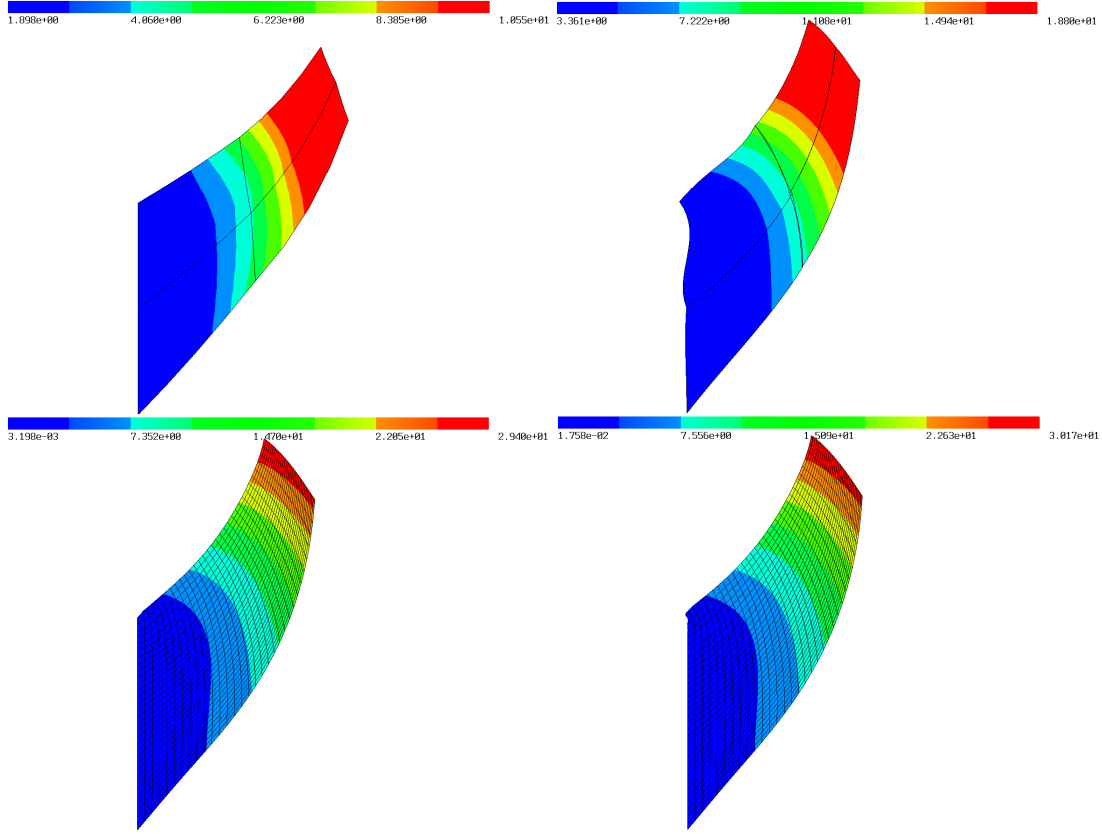


Figure 5.7: Final deformation for Cook's membrane example with $f = 32$ standard method (left) and \mathbf{F} -based method (right) for 2×2 (top) and 32×32 (bottom) grid.

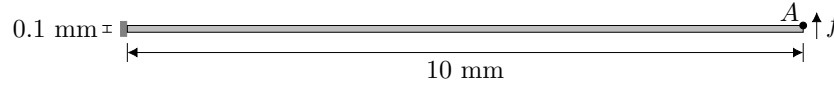


Figure 5.8: Geometry of thin beam example.

5.2.4 Inflation of a Hollow Spherical Ball

A hollow spherical ball is subjected to the boundary condition $u_{\text{in}} = (\gamma - 1)X$ on the inner boundary, whereas the outer boundary is left free. The inner and outer radius are given by $R_i = 0.5 \text{ mm}$ and $R_o = 1 \text{ mm}$, respectively. We adapted the benchmark in [40] by setting the material parameters $\mu = 1 \text{ N mm}^{-2}$ and $\lambda = 100 \text{ N mm}^{-2}$ together with the hyperelastic potential (5.2b) instead of using a complete incompressible material. This choice of λ , however, leads to a Poisson ratio $\nu = \frac{100}{202} \approx 0.495$ and thus, the example is already close to the nearly incompressible regime. The final configuration is reached for $\gamma = 3$, starting from $\gamma = 1$, the initial configuration. Due to symmetry, only one eighth of the ball is considered, see Figure 5.10. Unstructured curved tetrahedral meshes are used as shown in Figure 5.11.

We note that the standard method does not converge for polynomial order 2, whereas the \mathbf{F} - and \mathbf{FC} -based method do. Thus, only for the Lagrangian elements order 3 is considered. The \mathbf{C} -based method, however, does not converge - even with the stabilization terms (3.21) and (3.22). Although a higher polynomial order is used, the standard method does not perform as good as the \mathbf{F} - and \mathbf{FC} -based method for the coarse grid, cf. Figure 5.12. The results are listed in Table 5.5.

coupl. dof		w	$\ U\ $	w	$\ U\ $
		$f = 8$		$f = 16$	
std	32	5.767	86.168	9.902	153.983
	112	7.236	113.156	12.012	199.393
	416	7.992	128.938	13.281	232.024
	1600	8.290	135.377	13.794	246.522
	6272	8.403	137.821	13.977	252.014
F	60	8.554	141.578	14.299	261.363
	216	8.527	140.770	14.218	259.260
	816	8.514	140.441	14.188	258.691
	3168	8.509	140.312	14.195	259.070
	12480	8.507	140.282	14.201	259.345
C	60	8.230	134.535	13.872	249.196
	216	8.381	137.800	14.031	253.808
	816	8.444	139.029	14.094	255.716
	3168	8.475	139.577	14.123	256.705
	12480	8.489	139.854	14.142	257.391
FC	60	8.553	141.513	14.295	261.013
	216	8.522	140.635	14.205	258.870
	816	8.510	140.349	14.179	258.389
	3168	8.507	140.257	14.300	262.429
	12480	8.506	140.244	14.204	259.429

Table 5.2: Results for Cook’s membrane example for $f = 8$ and $f = 16$ with 2×2 , 4×4 , 8×8 , 16×16 , and 32×32 grids. For all methods the number of coupling dofs, the vertical deflection at point A and the L^2 norm of the displacement are presented.

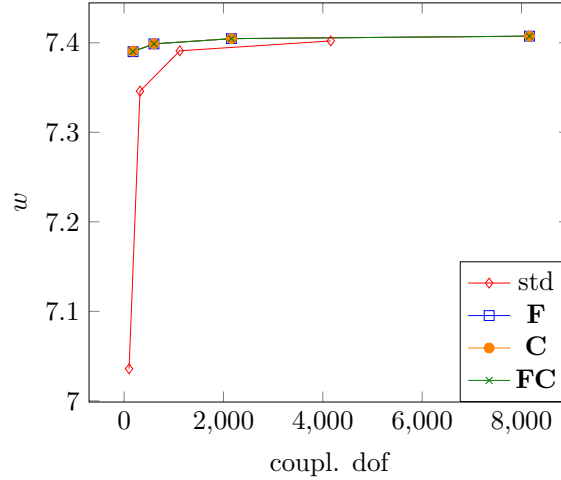


Figure 5.9: Vertical deflection of thin beam example at point A .

5.2.5 Cylindrical Shell

The benchmark presented in [35, 32] is adapted in terms of the force and boundary condition as line forces and traces are not well defined in terms of Sobolev spaces in three spatial dimensions. The same geometry and material parameters are considered. Namely, a quarter of a cylindrical structure with $r_i = 9 - t/2$ mm, $l = 15$ mm, and thickness $t = 2$ mm or 0.2 mm, see Figure 5.13, and $\mu = 6000 \text{ N mm}^{-2}$ and $\lambda = 24000 \text{ N mm}^{-2}$ together with the hyperelastic potential (5.2b). The structure is clamped at the bottom area and an area shear force $f = 240 \text{ N mm}^{-2}$ ($f = 2.7 \text{ N mm}^{-2}$

	coupl. dof	w	$\ U\ $	w	$\ U\ $
		$f = 24$		$f = 32$	
std	32	13.305	212.422	16.348	265.766
	112	15.579	269.195	18.574	329.713
	416	17.052	315.428	20.053	385.690
	1600	17.700	337.958	20.778	415.150
	6272	17.948	346.933	21.093	427.745
F	60	18.439	363.620	21.769	453.584
	216	18.317	359.827	21.639	448.622
	816	18.317	360.305	21.747	453.602
	3168	18.346	361.587	21.612	448.416
	12480	18.281	359.313	21.530	445.142
C	60	17.980	346.236	21.237	429.732
	216	18.109	351.697	21.354	436.172
	816	18.159	354.099	21.405	439.173
	3168	18.189	355.628	21.455	441.717
	12480	-	-	-	-
FC	60	18.424	362.626	21.734	451.528
	216	18.292	358.944	21.596	446.903
	816	18.584	370.337	21.769	455.071
	3168	18.345	361.562	21.573	446.896
	12480	18.265	358.718	21.531	445.182

Table 5.3: Results for Cook’s membrane example for $f = 24$ and $f = 32$ with 2×2 , 4×4 , 8×8 , 16×16 , and 32×32 grids. For all methods the number of coupling dofs, the vertical deflection at point A and the L^2 norm of the displacement are presented.

	coupl. dof	w	$\ U\ $	coupl. dof	w	$\ U\ $
	ne=10			ne=40		
std	100	7.036	3.992	320	7.346	4.273
F	180	7.390	4.314	600	7.399	4.321
C	180	7.391	4.314	600	7.399	4.321
FC	180	7.390	4.314	600	7.399	4.321
	ne=160			ne=640		
std	1120	7.391	4.314	4160	7.402	4.324
F	2160	7.405	4.326	8160	7.407	4.329
C	2160	7.405	4.326	8160	7.407	4.329
FC	2160	7.405	4.326	8160	7.407	4.329

Table 5.4: Results for thin beam example. For all methods the number of coupling dofs, the vertical deflection at point A and the L^2 norm of the displacement are given.

for $t = 0.2$ mm) is applied on the top. Structured hexahedra meshes with $8 \times 4 \times 1$, $16 \times 8 \times 1$, and $32 \times 16 \times 1$ grids are used, see Figure 5.14. For the standard method also a $64 \times 32 \times 1$ grid is used. The vertical deflection at point A is depicted in Figure 5.16, the final deformations are shown in Figure 5.15, and the results can be found in Table 5.6. We observed a locking behaviour for the standard method, which becomes significant for the small thickness. All of the three presented methods give satisfying results already for the coarsest discretization. The reference values were computed with the standard method and degree $k = 4$ on the finest grid, where locking is avoided due to the high polynomial degree. As only one layer in the thin direction is used the methods do not converge towards to reference solution for $t = 2$. For the thin structure, $t = 0.2$, the values match. As already mentioned the **F**-based method may suffer from a larger number of Newton iterations to reach convergence, whereas the **C**- and **FC**-based method have a better convergence

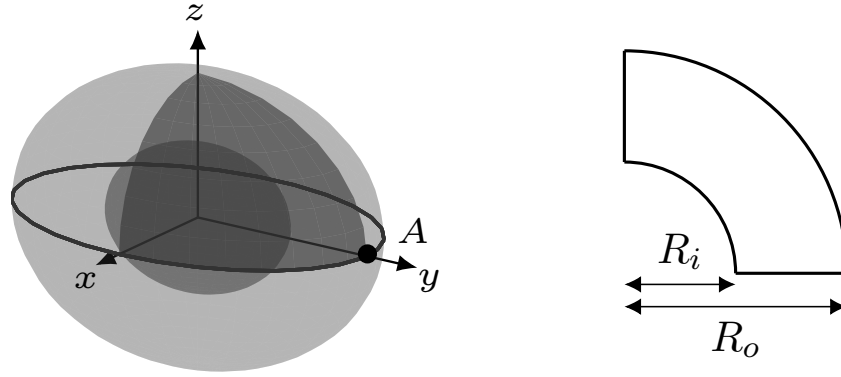


Figure 5.10: 3D geometry of inflation of a hollow spherical ball example and 2D cross-section.

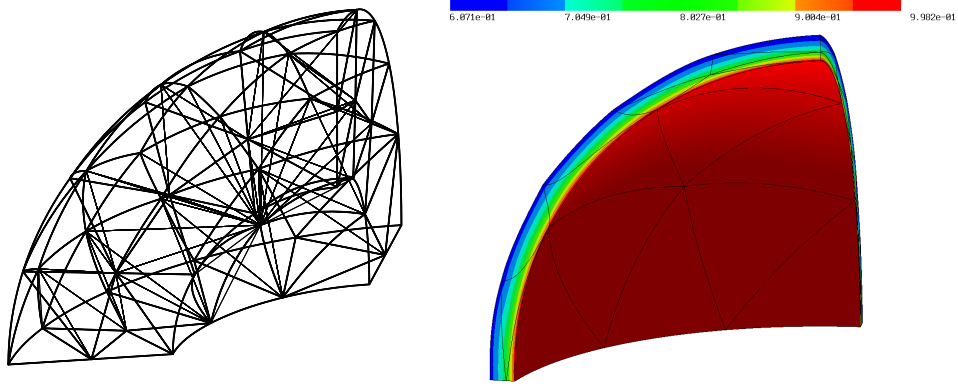


Figure 5.11: Curved mesh (left) and final configuration with 85 elements for inflation of a hollow spherical ball example.

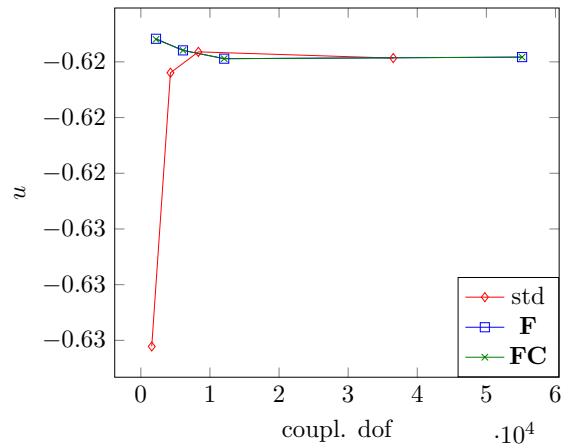


Figure 5.12: Radial deflection of inflation of a hollow spherical ball example at point A.

behavior. In Table 5.7 the numbers of Newton iterations can be found, where twelve load steps were considered. Also the standard method needs more iterations than the **C**- and **FC**-based variant.

	ne	dof	coupl. dof	w	$\ U\ $
std	85	1578	1578	-0.630	0.517
	244	4287	4287	-0.620	0.517
	494	8322	8322	-0.620	0.518
	2405	36528	36528	-0.620	0.518
F	85	17496	2196	-0.619	0.517
	244	50019	6099	-0.620	0.517
	494	100983	12063	-0.620	0.518
	2405	488073	55173	-0.620	0.518
FC	85	37896	2196	-0.619	0.517
	244	108579	6099	-0.620	0.517
	494	219543	12063	-0.620	0.518
	2405	1065273	55173	-0.620	0.518

Table 5.5: Results for inflation of a hollow spherical ball example. For all methods the number of elements, number of dofs and coupling dofs, the vertical deflection at point A and the L^2 norm of the displacement are given.

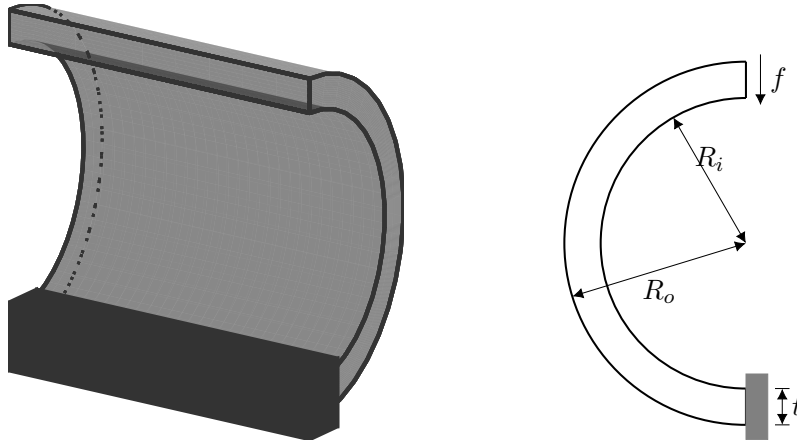


Figure 5.13: 3D geometry of cylindrical shell example and 2D cross-section.

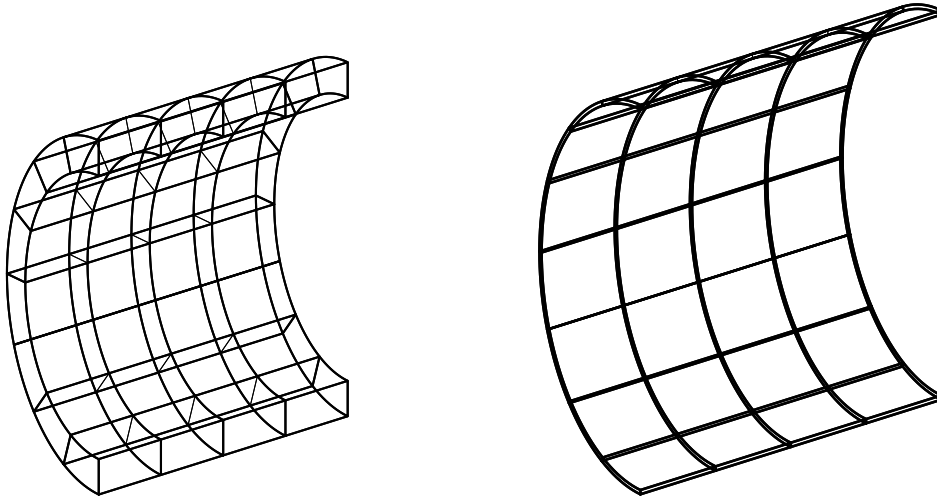


Figure 5.14: Curved meshes with $8 \times 4 \times 1$ grid for cylindrical shell example for $t = 2$ and $t = 0.2$.

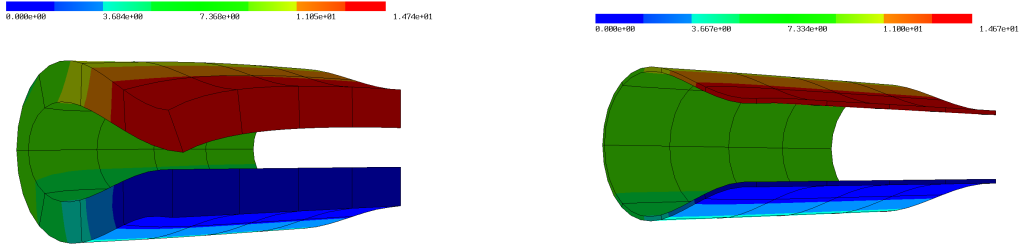


Figure 5.15: Final configuration of cylindrical shell example for $t = 2$ and $t = 0.2$ with $16 \times 8 \times 1$ grid.

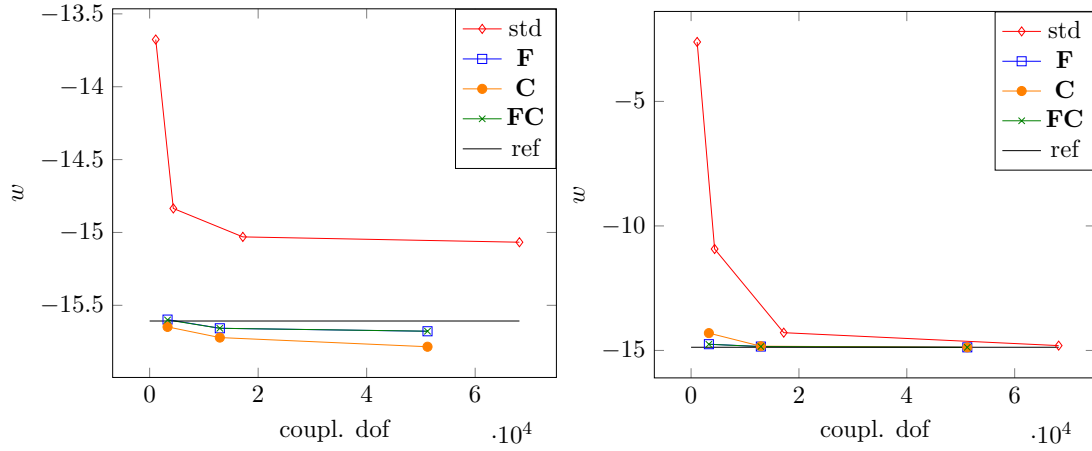


Figure 5.16: Vertical deflection of cylindrical shell example at point A.

	coupl. dof	w	$\ U\ $	w	$\ U\ $
		$t = 2$		$t = 0.2$	
std	1125	-13.676	211.958	-2.613	14.350
	4365	-14.835	231.071	-10.927	58.065
	17181	-15.030	234.734	-14.287	76.437
	68157	-15.067	235.513	-14.806	79.387
F	3300	-15.598	244.530	-14.749	78.920
	12936	-15.658	245.756	-14.844	79.571
	51216	-15.678	246.149	-14.876	79.825
C	300	-15.648	245.779	-14.304	76.878
	12936	-15.721	246.883	-14.830	79.521
	51216	-15.784	247.951	-14.876	79.825
FC	3300	-15.600	244.586	-14.753	78.946
	12936	-15.658	245.757	-14.844	79.576
	51216	-15.678	246.143	-14.876	79.825

Table 5.6: Results for cylindrical shell example. For all methods the number of coupling dofs, the vertical deflection at point A and the L^2 norm of the displacement are given.

5.2.6 Thin Beam subjected to end moment

For this example we use a cantilever beam, clamped at the left-hand side, of length $L = 100$ mm and thickness $t = 1$ mm. To allow for an analytical solution, we choose material parameters $\mu = 1 \times 10^4 \text{ N m}^{-2}$ and $\lambda = 0 \text{ N m}^{-2}$. An end moment is applied such that the beam cross-

t	std	F	C	FC
2	6	5	5	5
0.2	7	7-8	4-5	4-5

Table 5.7: Number of Newton iterations for $32 \times 16 \times 1$ grid in cylindrical shell example.

section rotates by 360° , thereby forming a perfect circle in the theory of thin shells. Due to the enormous deformation the Updated Lagrangian scheme discussed in Section 4 is used for all presented methods. Two different grids are used, where one element is used in thickness direction, and 10 or 20 elements in axial direction. The quantity of interest is given by the applied moment necessary to rotate the cross-section at the tip by 360° . In Figure 5.17 the final deformation is depicted and the results, as well as the absolute and relative error in the necessary moment as compared to the analytical value of $M_0 = \frac{4\pi\mu t^3}{12L} = 104.720 \text{ Nm}$ are given in Table 5.8. The **C**-based method did not converge for the coarsest grid and elements of order one, whereas the other two methods always converged. The overall accuracy of the methods is comparable. Concerning iteration counts, the **C**- and **FC**-based methods converged very fast, needing 3-7 iterations in each of the 12 load steps. In comparison, for the standard nodal FEM and the **F**-based methods, more than 20 iterations were necessary in some of the load steps.

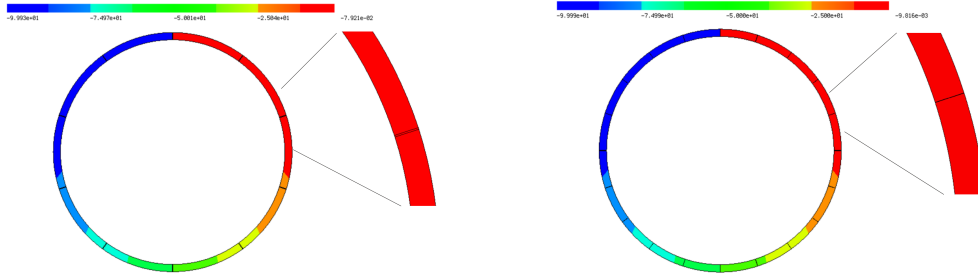


Figure 5.17: Displacement u_x in deformed geometry of thin beam subjected to end moment, **F**-based method, including zoom into element interface. Left: 10 elements, order $p = 1$; right: 20 elements, order $p = 2$.

	coupl. dof	moment	rel. error	coupl. dof	moment	rel. error
ne = 10	order 1			order 2		
std. method	40	5538.381	51.888	100	231.149	1.207314
F	120	103.172	-0.014781	180	104.685	-0.000330
C	120	—	—	180	104.744	0.000229
FC	120	101.399	-0.031715	180	104.679	-0.000385
ne = 20	order 1			order 2		
std	80	1425.993	12.617	200	113.175	0.080743
F	240	103.908	-0.007750	360	104.734	0.000138
C	240	104.668	-0.000498	360	104.738	0.000177
FC	240	103.878	-0.008038	360	104.734	0.000138

Table 5.8: Results for circular bending of a thin beam. For all methods, the end moment necessary to obtain a rotation of 360° is provided, as well as the relative error as compared to the analytical value of $M_0 = \frac{4\pi\mu t^3}{12L}$.

Acknowledgements

The support by the Austrian Science Fund (FWF) project W 1245 is gratefully acknowledged.

A Proof of consistency

We prove consistency of problem (3.16). If we take the variation of (3.17) in direction δu and look at the left-hand side

$$\sum_{T \in \mathcal{T}} \left(\int_T \mathbf{F}(u) \boldsymbol{\Sigma} : \nabla \delta u \, dX + \int_{\partial T} (\mathbf{F}(u) \boldsymbol{\Sigma})_{NN} \delta u_N - (\nabla \delta u \boldsymbol{\Sigma})_{NN} (u - \alpha)_N \, dS \right)$$

we want to recover the strong form if we insert the true, smooth solution \tilde{u} . First, the hybridization variable α is the normal trace of \tilde{u} and thus, $(\tilde{u} - \alpha)_N = 0$ on ∂T . Integration by parts and reordering yields

$$\begin{aligned} & \sum_{T \in \mathcal{T}} \left(\int_T -\operatorname{div}(\mathbf{F}(\tilde{u}) \boldsymbol{\Sigma}) \cdot \delta u \, dX + \int_{\partial T} ((\mathbf{F}(\tilde{u}) \boldsymbol{\Sigma})_N \delta u - (\mathbf{F}(\tilde{u}) \boldsymbol{\Sigma})_{NN} \delta u_N) \, dS \right) \\ &= \sum_{T \in \mathcal{T}} \left(\int_T -\operatorname{div}(\mathbf{F}(\tilde{u}) \boldsymbol{\Sigma}) \cdot \delta u \, dX + \int_{\partial T} (\mathbf{F}(\tilde{u}) \boldsymbol{\Sigma})_{NT} \cdot \delta u_T \, dS \right) \\ &= \sum_{T \in \mathcal{T}} \int_T -\operatorname{div}(\mathbf{F}(\tilde{u}) \boldsymbol{\Sigma}) \cdot \delta u \, dX + \sum_{E \in \mathcal{E}} \int_E [(\mathbf{F}(\tilde{u}) \boldsymbol{\Sigma})_{NE} \boldsymbol{\Sigma}] \cdot \delta u_{TE} \, dS. \end{aligned} \quad (\text{A.1})$$

The first term states the element wise balance equation $-\operatorname{div}(\mathbf{F}(\tilde{u}) \boldsymbol{\Sigma})|_T = f|_T$ and the second the continuity of the normal-tangential components of the first Piola–Kirchhoff stress tensor. Reordering hybridization terms in (3.17) yields

$$\sum_{E \in \mathcal{E}} \int_E [(\mathbf{F}(\tilde{u}) \boldsymbol{\Sigma})_{NE} \boldsymbol{\Sigma}] \delta \alpha_{NE} \, dS = 0 \quad (\text{A.2})$$

forcing the normal-normal continuity and thus, the continuity of the normal component of the first Piola–Kirchhoff stress tensor. Hence, also the interface condition is fulfilled and the problem is consistent.

B Linearization

Computing the first variations and under the assumption of small deformations, i.e., $u = \mathcal{O}(\varepsilon)$, $\nabla u = \mathcal{O}(\varepsilon)$, $\alpha = \mathcal{O}(\varepsilon)$, $\boldsymbol{\Sigma} = \mathcal{O}(\varepsilon)$, and $\mathbf{C}(u) = 2\varepsilon(u) + \mathbf{I} + \mathcal{O}(\varepsilon^2)$, the variations of (3.17) become

$$\int_{\Omega} \frac{\partial \Psi(\mathbf{E})}{\partial \mathbf{E}} : \delta \mathbf{E} - \boldsymbol{\Sigma} : \delta \mathbf{E} \, dX = 0 \quad \forall \delta \mathbf{E}, \quad (\text{B.1a})$$

$$- \sum_{T \in \mathcal{T}} \left(\int_T (\mathbf{E} - \varepsilon(u)) : \delta \boldsymbol{\Sigma} \, dX + \int_{\partial T} (\delta \boldsymbol{\Sigma})_{NN} (u - \alpha)_N \, dS \right) = 0 \quad \forall \delta \boldsymbol{\Sigma}, \quad (\text{B.1b})$$

$$\sum_{T \in \mathcal{T}} \left(\int_T \boldsymbol{\Sigma} : \nabla \delta u \, dX - \int_{\partial T} \boldsymbol{\Sigma}_{NN} \delta u_N \, dS \right) = \int_{\Omega} f \cdot \delta u \, dX \quad \forall \delta u, \quad (\text{B.1c})$$

$$\sum_{T \in \mathcal{T}} \int_{\partial T} \boldsymbol{\Sigma}_{NN} \delta \alpha_N \, dS = 0 \quad \forall \delta \alpha, \quad (\text{B.1d})$$

where we implicitly defined $\mathbf{E} := \frac{1}{2}(\mathbf{C} - \mathbf{I})$ and $\delta \mathbf{E} := \frac{1}{2} \delta \mathbf{C}$. Assuming a quadratic potential, i.e., $\frac{\partial \Psi}{\partial \mathbf{E}} = \mathbb{D} \mathbf{E}$, and eliminating \mathbf{E} by $\boldsymbol{\Sigma}$ with (B.1a) recovers the hybridized TDNNS method (2.4). Thus, the linearized versions of (3.17) and (3.6) coincide.

References

- [1] ANGOSHTARI, A., SHOJAEI, M. F., AND YAVARI, A. Compatible-strain mixed finite element methods for 2D compressible nonlinear elasticity. *Computer Methods in Applied Mechanics and Engineering* 313 (2017), 596–631.
- [2] ANGOSHTARI, A., AND YAVARI, A. Hilbert complexes of nonlinear elasticity. *Zeitschrift für angewandte Mathematik und Physik* 67, 6 (2016), 143.
- [3] ARNOLD, D., AWANOU, G., AND WINTHER, R. Finite elements for symmetric tensors in three dimensions. *Mathematics of Computation* 77, 263 (2008), 1229–1251.
- [4] ARNOLD, D., FALK, R., AND WINTHER, R. Mixed finite element methods for linear elasticity with weakly imposed symmetry. *Mathematics of Computation* 76, 260 (2007), 1699–1723.
- [5] ARNOLD, D. N., BREZZI, F., AND DOUGLAS, J. PEERS: a new mixed finite element for plane elasticity. *Japan Journal of Applied Mathematics* 1, 2 (1984), 347.
- [6] ARNOLD, D. N., AND WINTHER, R. Mixed finite elements for elasticity. *Numerische Mathematik* 92, 3 (2002), 401–419.
- [7] ARTIOLI, E., DA VEIGA, L. B., LOVADINA, C., AND SACCO, E. Arbitrary order 2D virtual elements for polygonal meshes: part II, inelastic problem. *Computational Mechanics* 60, 4 (2017), 643–657.
- [8] BAYAT, H. R., KRÄMER, J., WUNDERLICH, L., WULFINGHOFF, S., REESE, S., WOHLMUTH, B., AND WIENERS, C. Numerical evaluation of discontinuous and nonconforming finite element methods in nonlinear solid mechanics. *Computational Mechanics* 62, 6 (2018), 1413–1427.
- [9] BEIRÃO DA VEIGA, L., LOVADINA, C., AND MORA, D. A virtual element method for elastic and inelastic problems on polytope meshes. *Computer Methods in Applied Mechanics and Engineering* 295 (2015), 327–346.
- [10] BOFFI, D., BREZZI, F., AND FORTIN, M. *Mixed finite element methods and applications*, vol. 44. Springer, Berlin, Heidelberg, 2013.
- [11] BONET, J., GIL, A. J., AND ORTIGOSA, R. A computational framework for polyconvex large strain elasticity. *Computer Methods in Applied Mechanics and Engineering* 283 (2015), 1061–1094.
- [12] BONET, J., GIL, A. J., AND ORTIGOSA, R. On a tensor cross product based formulation of large strain solid mechanics. *International Journal of Solids and Structures* 84 (2016), 49–63.
- [13] BRAESS, D. *Finite elements: Theory, fast solvers, and applications in elasticity theory*, 3 ed. Cambridge University Press, 2007.
- [14] BREZZI, F., DOUGLAS, J., AND MARINI, L. D. Two families of mixed finite elements for second order elliptic problems. *Numerische Mathematik* 47, 2 (1985), 217–235.
- [15] CHEEGER, J., MÜLLER, W., AND SCHRADER, R. Kinematic and tube formulas for piecewise linear spaces. *Indiana University Mathematics Journal* 35, 4 (1986), 737–754.
- [16] CHI, H., DA VEIGA, L. B., AND PAULINO, G. Some basic formulations of the virtual element method (VEM) for finite deformations. *Computer Methods in Applied Mechanics and Engineering* 318 (2017), 148–192.
- [17] CHRISTIANSEN, S. H. On the linearization of Regge calculus. *Numerische Mathematik* 119, 4 (2011), 613–640.

- [18] COCKBURN, B., GOPALAKRISHNAN, J., AND LAZAROV, R. Unified hybridization of discontinuous Galerkin, mixed, and continuous Galerkin methods for second order elliptic problems. *SIAM Journal on Numerical Analysis* 47, 2 (2009), 1319–1365.
- [19] KASPER, E. P., AND TAYLOR, R. L. A mixed-enhanced strain method: Part I: Geometrically linear problems. *Computers & Structures* 75, 3 (2000), 237–250.
- [20] KASPER, E. P., AND TAYLOR, R. L. A mixed-enhanced strain method: Part II: Geometrically nonlinear problems. *Computers & Structures* 75, 3 (2000), 251–260.
- [21] LI, L. *Regge Finite Elements with Applications in Solid Mechanics and Relativity*. PhD thesis, University of Minnesota, 2018.
- [22] MEINDLHUMER, M., AND PECHSTEIN, A. 3D mixed finite elements for curved, flat piezoelectric structures. *International Journal of Smart and Nano Materials* 10, 4 (2019), 249–267.
- [23] MONK, P. *Finite element methods for Maxwell’s equations*. Numerical Mathematics and Scientific Computation. Oxford University Press, New York, 2003.
- [24] NÉDÉLEC, J. C. A new family of mixed finite elements in R3. *Numerische Mathematik* 50, 1 (1986), 57–81.
- [25] PECHSTEIN, A., AND SCHÖBERL, J. Tangential-displacement and normal-normal-stress continuous mixed finite elements for elasticity. *Mathematical Models and Methods in Applied Sciences* 21, 8 (2011), 1761–1782.
- [26] PECHSTEIN, A., AND SCHÖBERL, J. Anisotropic mixed finite elements for elasticity. *International Journal for Numerical Methods in Engineering* 90, 2 (2012), 196–217.
- [27] PECHSTEIN, A., AND SCHÖBERL, J. An analysis of the TDNNS method using natural norms. *Numerische Mathematik* 139, 1 (2018), 93–120.
- [28] PECHSTEIN, A. S. Large deformation mixed finite elements for smart structures. *Mechanics of Advanced Materials and Structures* 0, 0 (2019), 1–11.
- [29] PFEFFERKORN, R., AND BETSCH, P. Extension of the enhanced assumed strain method based on the structure of polyconvex strain-energy functions. *International Journal for Numerical Methods in Engineering* 121, 8 (2020), 1695–1737.
- [30] RAVIART, P.-A., AND THOMAS, J.-M. A mixed finite element method for 2-nd order elliptic problems. In *Mathematical Aspects of Finite Element Methods*, vol. 66. Springer, 1977, pp. 292–315.
- [31] REDDY, B., AND SIMO, J. Stability and convergence of a class of enhanced strain methods. *SIAM Journal on Numerical Analysis* 32, 6 (1995), 1705–1728.
- [32] REESE, S. On the equivalent of mixed element formulations and the concept of reduced integration in large deformation problems. *International Journal of Nonlinear Sciences and Numerical Simulation* 3, 1 (2002), 1–34.
- [33] REESE, S. A large deformation solid-shell concept based on reduced integration with hourglass stabilization. *International Journal for Numerical Methods in Engineering* 69, 8 (2007), 1671–1716.
- [34] REESE, S., BAYAT, H., AND WULFINGHOFF, S. On an equivalence between a discontinuous Galerkin method and reduced integration with hourglass stabilization for finite elasticity. *Computer Methods in Applied Mechanics and Engineering* 325 (2017), 175–197.
- [35] REESE, S., WRIGGERS, P., AND REDDY, B. A new locking-free brick element technique for large deformation problems in elasticity. *Computers & Structures* 75, 3 (2000), 291–304.

- [36] REGGE, T. General relativity without coordinates. *Il Nuovo Cimento (1955-1965)* 19, 3 (1961), 558–571.
- [37] SCHÖBERL, J. NETGEN an advancing front 2D/3D-mesh generator based on abstract rules. *Computing and Visualization in Science* 1, 1 (1997), 41–52.
- [38] SCHÖBERL, J. C++ 11 implementation of finite elements in NGSolve. *Institute for Analysis and Scientific Computing, Vienna University of Technology* (2014).
- [39] SCHRÖDER, J., WRIGGERS, P., AND BALZANI, D. A new mixed finite element based on different approximations of the minors of deformation tensors. *Computer Methods in Applied Mechanics and Engineering* 200, 49 (2011), 3583–3600.
- [40] SHOJAEI, M. F., AND YAVARI, A. Compatible-strain mixed finite element methods for 3D compressible and incompressible nonlinear elasticity. *Computer Methods in Applied Mechanics and Engineering* 357 (2019), 112610.
- [41] SIMO, J., ARMERO, F., AND TAYLOR, R. Improved versions of assumed enhanced strain trilinear elements for 3D finite deformation problems. *Computer Methods in Applied Mechanics and Engineering* 110, 3 (1993), 359–386.
- [42] SIMO, J., TAYLOR, R., AND PISTER, K. Variational and projection methods for the volume constraint in finite deformation elasto-plasticity. *Computer Methods in Applied Mechanics and Engineering* 51, 1 (1985), 177–208.
- [43] SIMO, J. C., AND ARMERO, F. Geometrically non-linear enhanced strain mixed methods and the method of incompatible modes. *International Journal for Numerical Methods in Engineering* 33, 7 (1992), 1413–1449.
- [44] SIMO, J. C., AND RIFAI, M. S. A class of mixed assumed strain methods and the method of incompatible modes. *International Journal for Numerical Methods in Engineering* 29, 8 (1990), 1595–1638.
- [45] SINWEL, A. *A New Family of Mixed Finite Elements for Elasticity*. PhD thesis, Johannes Kepler University Linz, 2009.
- [46] STENBERG, R. A family of mixed finite elements for the elasticity problem. *Numerische Mathematik* 53, 5 (1988), 513–538.
- [47] WASHIZU, K. *Variational methods in elasticity and plasticity*, vol. 3. Pergamon press Oxford, 1975.
- [48] WRIGGERS, P., REDDY, B., RUST, W., AND HUDOBIVNIK, B. Efficient virtual element formulations for compressible and incompressible finite deformations. *Computational Mechanics* 60, 2 (2017), 253–268.
- [49] WULFINGHOFF, S., BAYAT, H. R., ALIPOUR, A., AND REESE, S. A low-order locking-free hybrid discontinuous Galerkin element formulation for large deformations. *Computer Methods in Applied Mechanics and Engineering* 323 (2017), 353–372.
- [50] ZAGLMAYR, S. *High Order Finite Element Methods for Electromagnetic Field Computation*. PhD thesis, Johannes Kepler Universität Linz, 2006.
- [51] ZIENKIEWICZ, O., AND TAYLOR, R. *The Finite Element Method. Vol. 1: The Basis*, 5 ed. Butterworth-Heinemann, 2000.